

Oblique transition in hypersonic double-wedge flow: An input-output viewpoint

Anubhav Dwivedi^{1†}, G. S. Sidharth², Mihailo R. Jovanović¹

¹Ming-Hsieh Department of Electrical and Computer Engineering, Los Angeles, CA, USA

²X-Computational Physics, Los Alamos National Laboratory, NM, USA

(Received xx; revised xx; accepted xx)

We utilize input-output and weakly nonlinear analyses in combination with direct numerical simulations (DNS) to identify mechanisms for oblique transition in a Mach 5 hypersonic flow over an adiabatic slender double-wedge. Even though the laminar separated flow is globally stable, input-output analysis demonstrates significant amplification of unsteady external disturbances. These disturbances are introduced upstream of the separation zone and they lead to the appearance of oblique waves further downstream. We demonstrate that large amplification of oblique waves arises from interactions of the fluctuation shear stress with streamline curvature of the laminar base flow in the separated shear layer. This is in contrast to the attached boundary layers, where no such mechanism exists. We also use a weakly nonlinear analysis to show that the resolvent operator associated with linearization around the laminar base flow governs the evolution of steady reattachment streaks that arise from quadratic interactions of unsteady oblique waves. These quadratic interactions generate vortical excitations in the reattaching shear layer which lead to the formation of streaks in the recirculation zone and their subsequent amplification, breakdown, and transition to turbulence downstream. Our analysis of the energy budget shows that deceleration of the base flow near reattachment is primarily responsible for amplification of steady streaks. Finally, we employ DNS to examine latter stages of transition to turbulence and demonstrate the predictive power of input-output framework in uncovering triggering mechanisms for oblique transition in separated high-speed boundary layer flows.

1. Introduction

Slender double-wedges are commonly encountered in intakes, control surfaces, and junctions in high-speed supersonic and hypersonic vehicles (Dolling 2001). In this geometry, laminar boundary layer can separate at the corner because of the pressure rise that arises from deflection of the inviscid free stream. The resulting flow is characterized by separation-reattachment shocks as well as a small recirculation zone and it provides a canonical setup for studying shock-wave-boundary-layer interaction (SWBLI) (Simeonides & Haase 1995). In spite of spanwise homogeneity of nominally two-dimensional (2D) flows over compression corners, both experiments (Chuvakhov *et al.* 2017; Roghelia *et al.* 2017; Dwivedi *et al.* 2020a) and numerical simulations (Navarro-Martinez & Tutty 2005; Dwivedi *et al.* 2017) identify three-dimensional (3D) features in time-averaged separated flow. In particular, streamwise streaks associated with persistent local peaks of heat flux or wall temperature, that appear near reattachment, can trigger transition to turbulence downstream (Simeonides & Haase 1995; Roghelia *et al.* 2017).

The development of 3D flow structures in hypersonic flows was recently studied by examining the growth of small perturbations in the presence of a recirculation

† Email address for correspondence: anubhavd91@gmail.com

zone (Dwivedi 2020). For example, 2D SWBLI becomes unstable inside the separation bubble when the strength of interaction increases beyond a critical value (Sidharth *et al.* 2017). The spanwise modulation that arises from global instability introduces streaks over compression corners (Sidharth *et al.* 2018) and oblique shocks impinging on a flat plate (Hildebrand *et al.* 2018). Even in the absence of global instability, high-speed separated flows are extremely sensitive to upstream vortical disturbances (Dwivedi *et al.* 2019) and small fluctuations around the laminar 2D base flow can experience significant non-modal amplification that leads to the appearance of steady reattachment streaks (Dwivedi *et al.* 2020b). Furthermore, recent experiments on the cone-flare configurations (Benitez *et al.* 2020; Butler & Laurence 2021), which represent axisymmetric counterparts of slender double-wedges, identify unsteady perturbations in the separation zone. These perturbations are significantly amplified in the recirculation zone and they play an important role in transition to turbulence (Butler & Laurence 2021).

In this paper, we examine amplification of unsteady fluctuations around the laminar 2D base flow in the separation/reattachment zone and investigate subsequent transition to turbulence. Free-stream disturbances (Choudhari 1996; Berlin & Henningson 1999; Maslov *et al.* 2001) that arise from wind tunnel noise in ground experiments (Schneider 2015) or from atmospheric disturbances in free flights (Bushnell 1990; Skinner *et al.* 2020) can lead to the appearance of unsteady fluctuations in boundary layer flows. Even though the importance of these fluctuations in initiating transition in attached high-speed boundary layers received significant attention (Ma & Zhong 2005; Sivasubramanian & Fasel 2015; Hader & Fasel 2019), their role in separated high-speed flows has not been studied before. Recent experiments (Benitez *et al.* 2020) suggest that their amplification within the recirculation zone can trigger unsteadiness in transitional SBWLI flows. We utilize a global input-output analysis to quantify amplification of unsteady upstream disturbances in a Mach 5 flow over a slender double-wedge and characterize their role in initiating transition to turbulence in high-speed separated boundary layer flows.

Input-output analysis provides a framework for evaluating responses (outputs) of stable dynamical systems to external disturbances (inputs). For time-independent globally stable base flows, the steady-state response of the linearized Navier-Stokes (NS) equations to a harmonic input with frequency ω is also harmonic with the same frequency and the frequency response maps the input forcing to the resulting steady-state output (Jovanović 2004; Jovanović & Bamieh 2005; Jovanović 2021). The singular value decomposition (SVD) of the frequency response characterizes amplification across frequency ω and decomposes inputs and outputs into modes whose significance is ordered by the magnitude of the corresponding singular values (Schmid 2007). In addition to providing insights into dynamics of canonical incompressible flows of Newtonian fluids (Jovanović & Bamieh 2005; Sipp & Marquet 2013; Ran *et al.* 2019a,b), input-output analysis has also been utilized to discover mechanisms for transition in complex fluids and complex flows, including transition to elastic turbulence in viscoelastic fluids (Hoda *et al.* 2008, 2009; Jovanović & Kumar 2011), noise generation in turbulent jets (Jeun *et al.* 2016), and the appearance of reattachment streaks in hypersonic flows (Dwivedi *et al.* 2019).

In addition to quantifying amplification of external disturbances and identifying spatial structure of strongly amplified input-output pairs, we also carry out analysis of the transport equation associated with the energy of flow fluctuations to uncover physical mechanisms responsible for amplification of oblique waves. We demonstrate that concave curvature of the separated/reattaching laminar base flow is primarily responsible for strong amplification of oblique fluctuations in the separation zone.

Oblique waves represent a potent mechanism for generation of steady 3D streaks in canonical low-speed incompressible (Berlin *et al.* 1999) and compressible (Chang & Malik

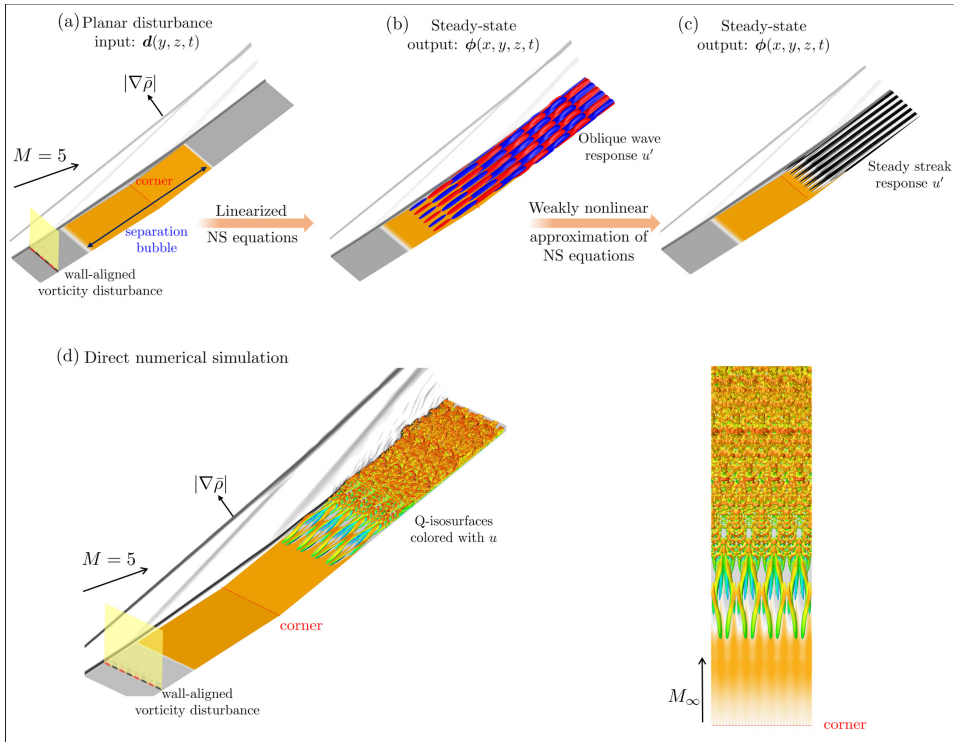


FIGURE 1. Preview of key results: (a) unsteady upstream forcing triggers (b) oblique waves in the separated shear layer and their quadratic interactions lead to the appearance of (c) steady streamwise streaks further downstream. (d) Direct numerical simulations validate our theoretical predictions and demonstrate the efficacy of unsteady oblique fluctuations in triggering transition to turbulence in separated high-speed boundary layer flows.

1994; Mayer *et al.* 2011) boundary layers. For a high-speed separated flow subject to unsteady upstream disturbances, we utilize a weakly nonlinear analysis to demonstrate that quadratic interactions of oblique waves generate vortical excitations that induce reattachment streaks in the recirculation zone. We also show that the resolvent operator associated with linearization around the laminar 2D base flow governs the evolution of steady reattachment streaks and utilize SVD to demonstrate that the streaks are well approximated by the second output mode of the resolvent. Our analysis of the energy budget shows that the base flow deceleration near reattachment is primarily responsible for amplification of reattachment streaks associated with this sub-optimal mode.

We also conduct direct numerical simulations (DNS) to confirm the predictive power of input-output and weakly nonlinear analyses and provide insight into latter stages of transition. Our simulations demonstrate that spanwise oscillations of streaks lead to the formation of 3D flow structures that cause breakdown and transition to turbulence downstream. We show that typical turbulent correlations do not hold in the transitional zone and demonstrate that unsteady oblique disturbances can indeed trigger transition to turbulence in separated high-speed flows. Our work provides a detailed characterization of transition initiated by a non-modal amplification of oblique waves whose nonlinear interactions lead to the appearance of steady reattachment streaks in the recirculation zone and their subsequent breakdown/transition to turbulence downstream; see figure 1 for an illustration.

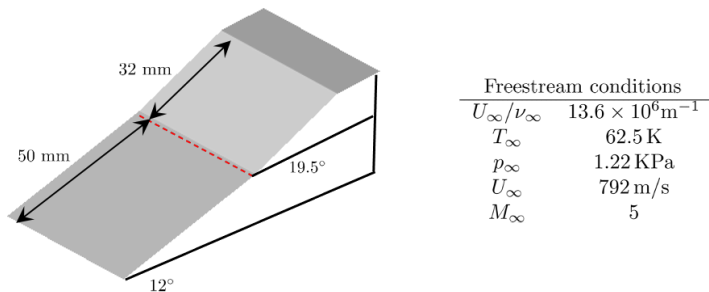


FIGURE 2. Slender double-wedge geometry and the associated free-stream conditions.

Our presentation is organized as follows. In § 2, we describe the slender double-wedge geometry along with a finite-volume compressible flow solver that we use in our computations. In § 3, we provide a brief summary of input-output analysis that we use to evaluate frequency responses of the double-wedge flow in the presence of 3D disturbances. We demonstrate large amplification of unsteady oblique waves and identify underlying physical mechanisms. In § 4, we employ a weakly nonlinear analysis to demonstrate that quadratic interactions of oblique waves induce steady reattachment streaks and discuss physical mechanism responsible for their amplification in recirculation zone. In § 5, we employ DNS to validate utility of our theoretical predictions and examine latter stages of transition induced by unsteady upstream disturbances. In § 6, we analyze statistical features of the resulting transitional and turbulent boundary layers. We provide summary of our contributions in § 7 and offer concluding remarks in § 8.

2. Hypersonic flow over an adiabatic slender double-wedge

Hypersonic flow over a slender double-wedge with free-stream conditions shown in figure 2 corresponds to the experiments of Yang *et al.* (2012). Since the enthalpy and the temperature in the flow field are low, we utilize the ideal gas law abstraction and employ the finite-volume compressible flow solver US3D (Candler *et al.* 2015) to compute the solution of the compressible NS equations in conservative form

$$\frac{\partial \mathbf{U}}{\partial t} + \frac{\partial \mathbf{F}_j}{\partial x_j} = 0, \quad (2.1)$$

where $\mathbf{F}_j(\mathbf{U})$ is the flux vector and $\mathbf{U} = (\rho, \rho \mathbf{u}, E)$ is the vector of conserved variables that represent density, momentum, and total energy per unit volume of the gas. We discretize the inviscid fluxes by employing the second-order-accurate modified Steger-Warming fluxes with the MUSCL limiters (Candler *et al.* 2015). In previous studies, the numerical method for the computation of the base state was validated using hypersonic double-wedge and double-cone setups (Nompelis *et al.* 2003; Nompelis & Candler 2009). The laminar 2D base flow is computed as the steady-state solution of equation (2.1) by implicit time-marching with 249 cells in the wall-normal and 535 cells in the streamwise direction. As illustrated in our previous work (Sidharth *et al.* 2018), this resolution is sufficient to capture separated flow and resolve the evolution of small perturbations.

Figure 3 shows the contours of density gradient magnitude on the compression corner. For the conditions provided in figure 2, the boundary layer separates around 13.8 mm from the corner on the first wedge and is associated with formation of the separation shock. The δ_{99} -thickness of the boundary layer near the separation location is about 1 mm. Unless otherwise specified, the length and the time scales are respectively non-

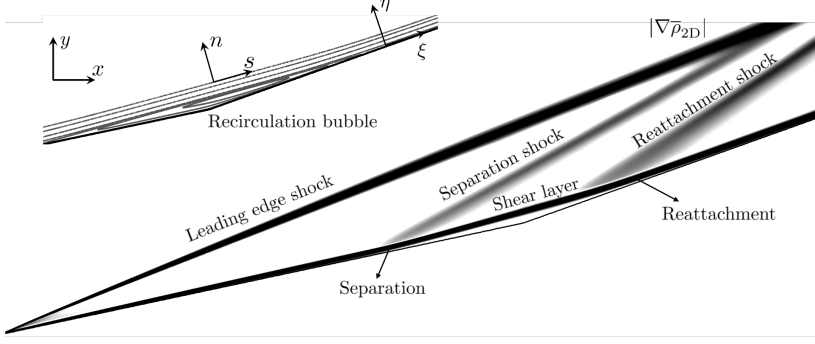


FIGURE 3. Contours of density gradient magnitude. The inset illustrates zoomed in view of the separation bubble and the schematic of various coordinate systems associated with the double-wedge geometry.

dimensionalized by δ_{99} at separation and by δ_{99}/U_∞ . The separated shear layer reattaches around 10.5 mm downstream of the corner on the second wedge and the reattaching shear layer is associated with the formation of the reattachment shock. The separation and the reattachment location in the laminar 2D flow are marked by S and R, respectively. Figure 3 also shows an inset of the separation zone along with the wall-aligned coordinate system (where ξ and η denote directions that are parallel and perpendicular to the wall) and a coordinate system that is locally aligned with the streamlines of the laminar 2D flow. Both coordinate systems are used in our study of the evolution of flow fluctuations.

Sidharth *et al.* (2018) demonstrated global linear stability of the laminar 2D separated base flow. Recent studies of similar SWBLI configurations, such as compression ramps, revealed extreme sensitivity to upstream disturbances even in the absence of global instability (Dwivedi *et al.* 2019). Leading-edge roughness and free-stream disturbances provide persistent sources of external excitation and they are inevitable in realistic flows. To evaluate the role of such uncertainty in triggering early stages of transition to turbulence, we utilize input-output analysis (Jovanović 2021) to quantify amplification of unsteady disturbances in a hypersonic flow over slender double-wedge.

3. Input-output analysis of a high-speed double-wedge flow

In this section, we employ input-output analysis to quantify amplification of unsteady external disturbances in globally stable 2D SWBLI over a slender double-wedge and uncover physical mechanisms that trigger early stages of transition to turbulence.

3.1. Amplification of exogenous disturbances

To account for the rate of change of perturbation density, momentum, and total energy, we model unsteady external disturbances as volumetric sources of excitation,

$$\mathbf{d}(\mathbf{x}, t) = \epsilon \mathbf{d}^{(1)}(\mathbf{x}, t), \quad (3.1)$$

and decompose the state variable $\mathbf{U} = (\rho, \rho \mathbf{u}, E)$ into the mean and fluctuating parts,

$$\mathbf{U}(\mathbf{x}, t) = \mathbf{U}^{(0)}(\mathbf{x}) + \epsilon \mathbf{U}^{(1)}(\mathbf{x}, t) + \epsilon^2 \mathbf{U}^{(2)}(\mathbf{x}, t) + \dots \quad (3.2)$$

Here, $\mathbf{U}^{(0)}(\mathbf{x})$ represents the laminar 2D base flow, \mathbf{x} is the vector of spatial coordinates, ϵ is a small amplitude, and the linearized flow equations

$$\left[\frac{\partial}{\partial t} - \mathcal{A}(\mathbf{U}^{(0)}) \right] \mathbf{U}^{(1)} = \mathcal{B} \mathbf{d}^{(1)}, \quad (3.3)$$

are obtained by neglecting $\mathcal{O}(\epsilon^2)$ terms upon substitution of (3.1) and (3.2) in the compressible NS equations. The compressible NS operator resulting from linearization around the base flow $\mathbf{U}^{(0)}$ is given by $\mathcal{A}(\mathbf{U}^{(0)})$ (Sidharth *et al.* 2018, equations (12)-(15)) and \mathcal{B} is the operator that specifies how disturbances enter into equation (3.3) that governs the evolution of small fluctuations $\mathbf{U}^{(1)}(\mathbf{x}, t)$ around $\mathbf{U}^{(0)}(\mathbf{x})$.

A second-order central finite-volume discretization (Sidharth *et al.* 2018) is used to obtain a finite dimensional approximation of equation (3.3) in conserved variables. The state-space formulation,

$$\begin{aligned} \frac{d}{dt} \mathbf{q} &= \mathbf{A} \mathbf{q} + \mathbf{B} \mathbf{d}, \\ \phi &= \mathbf{C} \mathbf{q}, \end{aligned} \quad (3.4)$$

describes the evolution of the spatially discretized perturbation vector \mathbf{q} , where \mathbf{d} is a spatially distributed and temporally varying disturbance (input) and ϕ is the quantity of interest (output). In equation (3.4) the matrix \mathbf{B} specifies how the input enters into the state equation, while the matrix \mathbf{C} extracts the output from the state vector \mathbf{q} . An input-output relation is obtained by applying the Laplace transform to equation (3.4),

$$\phi(s) = \mathbf{C}(s\mathbf{I} - \mathbf{A})^{-1}(\mathbf{q}(0) + \mathbf{B}\mathbf{d}(s)), \quad (3.5)$$

where $\mathbf{q}(0)$ denotes the initial condition and s is the complex number. Equation (3.5) can be used to characterize both the unforced (to initial condition $\mathbf{q}(0)$) and forced (to external disturbances \mathbf{d}) responses of flow fluctuations.

In boundary layer flows, the linearized system is globally stable and for a time-periodic input with frequency ω , $\mathbf{d}(t) = \hat{\mathbf{d}}(\omega)e^{i\omega t}$, the steady-state output of (3.4) is determined by $\phi(t) = \hat{\phi}(\omega)e^{i\omega t}$, where $\hat{\phi}(\omega) = \mathbf{H}(i\omega)\hat{\mathbf{d}}(\omega)$, $\mathbf{H}(i\omega)$ is the frequency response

$$\mathbf{H}(i\omega) = \mathbf{C}(i\omega\mathbf{I} - \mathbf{A})^{-1}\mathbf{B}, \quad (3.6)$$

and $\mathbf{R}(i\omega) = (i\omega\mathbf{I} - \mathbf{A})^{-1}$ is the resolvent associated with the linearized model (3.4). At any ω , the singular value decomposition of $\mathbf{H}(i\omega)$ can be used to quantify amplification of time-periodic inputs (Jovanović 2004; Schmid 2007; Jovanović 2021),

$$\hat{\phi}(\omega) = \mathbf{H}(i\omega)\hat{\mathbf{d}}(\omega) = \sum_i \sigma_i(\omega) \phi_i(\omega) \langle \mathbf{d}_i(\omega), \hat{\mathbf{d}}(\omega) \rangle_E. \quad (3.7)$$

Here, $\sigma_i(\omega)$ denotes the i th singular value of $\mathbf{H}(i\omega)$, $\langle \cdot, \cdot \rangle_E$ is the inner product that induces a compressible energy norm (Hanifi *et al.* 1996) (see appendix A), and $\mathbf{d}_i(\omega)$ and $\phi_i(\omega)$ are the left and right singular vectors of $\mathbf{H}(i\omega)$ which provide orthonormal bases of the corresponding input and output spaces (with respect to $\langle \cdot, \cdot \rangle_E$). The frequency response $\mathbf{H}(i\omega)$ maps the i th input mode $\mathbf{d}_i(\omega)$ into the response whose spatial profile is specified by the i th output mode $\phi_i(\omega)$ and the amplification is determined by the corresponding singular value $\sigma_i(\omega)$; i.e., for $\hat{\mathbf{d}}(\omega) = \mathbf{d}_i(\omega)$, $\hat{\phi}(\omega) = \mathbf{H}(i\omega)\mathbf{d}_i(\omega) = \sigma_i(\omega)\phi_i(\omega)$ and $\|\hat{\phi}(\omega)\|_E = \sigma_i(\omega)$.

For a given frequency ω , we use a matrix-free Arnoldi iterations (Jeun *et al.* 2016; Dwivedi 2020) to compute the singular values $\sigma_i(\omega)$ of $\mathbf{H}(i\omega)$. Note that, at any ω ,

$$G(\omega) := \sigma_1(\omega) = \frac{\|\mathbf{H}(i\omega)\mathbf{d}_1(\omega)\|_E}{\|\mathbf{d}_1(\omega)\|_E} = \frac{\|\sigma_1(\omega)\phi_1(\omega)\|_E}{\|\mathbf{d}_1(\omega)\|_E}, \quad (3.8)$$

determines the largest induced gain with respect to a compressible energy norm, where $(\mathbf{d}_1(\omega), \phi_1(\omega))$ identify the spatial structure of the dominant input-output pair.

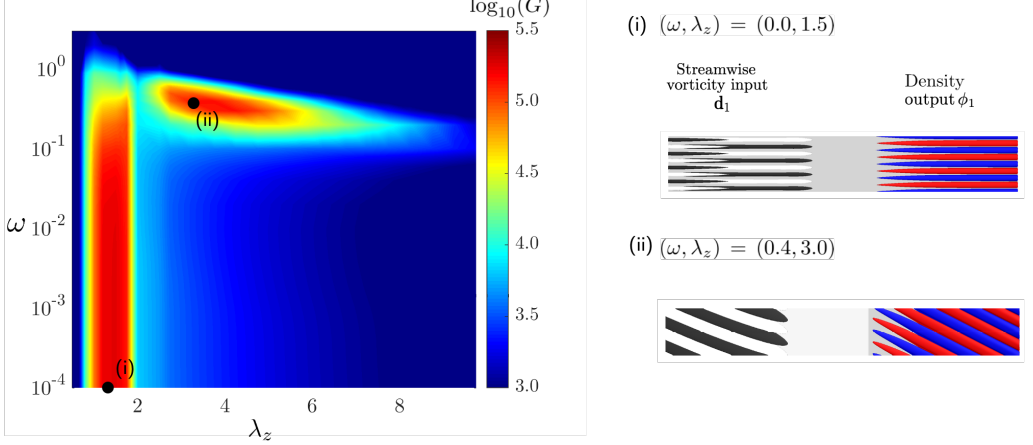


FIGURE 4. (a) Input-output gain $G(\omega, \lambda_z)$ associated with the resolvent operator across temporal frequency ω and spanwise wavelength λ_z . (b) Isosurfaces of streamwise vorticity and density fluctuations corresponding to the input-output modes \mathbf{d}_1 and ϕ_1 , respectively.

3.2. Frequency response analysis

We utilize input-output analysis to study amplification of harmonic disturbances with frequency ω . Owing to homogeneity in the spanwise direction, the 3D fluctuations in (3.3) take the form,

$$\mathbf{U}^{(1)}(x, y, z, t) = \hat{\mathbf{U}}^{(1)}(x, y, \beta, \omega) e^{i(\beta z + \omega t)}, \quad (3.9)$$

where $\beta = 2\pi/\lambda_z$ is the spanwise wavenumber. Thus, in addition to ω , the frequency response in equation (3.6) is also parameterized by the spanwise wavelength λ_z .

The input matrix \mathbf{B} specifies spatial support of body forcing inputs and the output matrix \mathbf{C} determines quantity of interest over a certain region (Jovanović 2021). We first set $\mathbf{B} = \mathbf{C} = \mathbf{I}$, i.e., we introduce inputs that excite flow at any spatial location and examine their impact on flow fluctuations in the entire computational domain. In this case, $\mathbf{H}(i\omega) = \mathbf{R}(i\omega)$ and we conduct the resolvent analysis using a resolution that yields grid-independent outputs with 545 cells in the streamwise, 249 cells in the wall-normal direction, and numerical sponge boundary conditions near the leading edge ($x = 1$) and the outflow boundaries.

Figure 4 shows the dependence of the input-output gain $G(\omega, \lambda_z)$ on the frequency ω and the wavelength λ_z . There are two major amplification regions with the respective peaks at $(\omega = 0, \lambda_z = 1.5)$ and $(\omega = 0.4, \lambda_z = 3)$. The first peak in G identifies the largest amplification and the corresponding output is determined by reattachment streaks that result from steady vortical disturbances upstream of the recirculation zone. We observe selective amplification of disturbances with $\lambda_z \approx 1.5$ and low-pass filtering features over ω . The input-output gain G experiences rapid decay beyond the roll-off frequency $\omega \approx 0.4$ and it attains its largest value at $\omega = 0$ for λ_z that scales with the reattaching shear layer thickness (Dwivedi *et al.* 2019). In contrast to Dwivedi *et al.* (2019), which focused on disturbances with $\omega = 0$, we examine unsteady disturbances that trigger oblique waves in the reattaching shear layer, as identified by the second peak in G . This amplification region takes place in a narrow band of temporal frequencies ω over a fairly broad range of spanwise wavelengths λ_z .

Even when we allow disturbances to enter through the entire computational domain, the largest amplification is caused by inputs that are localized upstream (near the

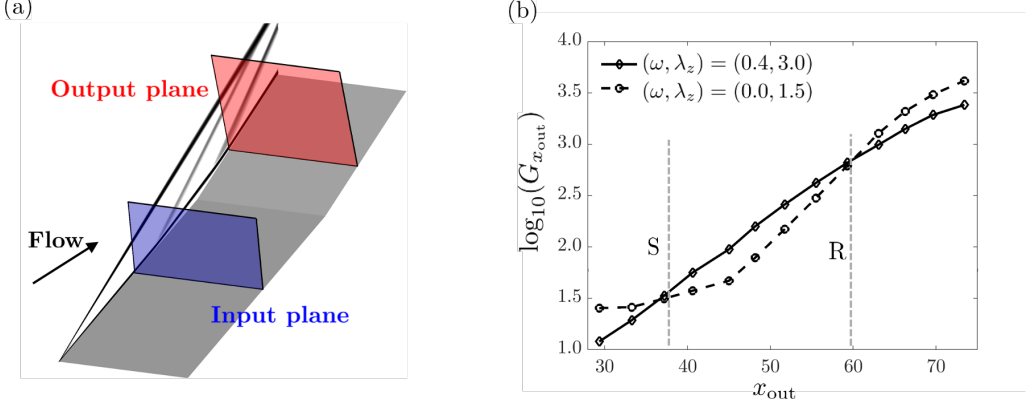


FIGURE 5. Spatial input-output analysis: (a) input is introduced at a streamwise location before separation and output is evaluated at x_{out} ; (b) dependence of the input-output gain $G_{x_{out}}$ on the streamwise location x_{out} for streaks and oblique waves. Unsteady oblique waves with $(\omega = 0.4, \lambda_z = 3)$ are strongly amplified throughout the separation zone.

inflow) with the resulting response appearing downstream. The upstream disturbances are most effective way to excite the flow because of large convection velocity of the mean flow (Chomaz 2005; Schmid 2007) and the dominant output emerges in the separated and the reattached regions of the base flow. To evaluate amplification in different spatial regions, we restrict inputs and outputs to belong to a plane. As illustrated in figure 5(a), this is accomplished via a proper selection of matrices \mathbf{B} and \mathbf{C} by fixing the input location before flow separation, at $x_{in} = 25$, and by evaluating the output at different downstream locations, x_{out} . In this setup, the input-output gain $G_{x_{out}}$ quantifies the largest amplification at x_{out} of disturbances which are introduced at $x_{in} = 25$.

Figure 5(b) shows $G_{x_{out}}$ for disturbances with $(\omega = 0, \lambda_z = 1.5)$ and $(\omega = 0.4, \lambda_z = 3)$. The gain associated with the steady perturbations begins to grow in the latter half of the recirculation zone, especially near the reattachment location. In contrast, unsteady perturbations with $\omega = 0.4$ exhibit significant amplification throughout the separation zone. This observation suggests that the separation zone plays a critical role in the amplification of unsteady flow fluctuations.

3.3. Amplification of oblique waves: physical mechanism

To analyze physical mechanisms responsible for amplification of oblique waves in the separation zone, we examine the spatial development of kinetic energy of flow fluctuations which undergo largest amplification at reattachment. In particular, we restrict the input at a plane $x_{in} = 25$ (prior to separation) and study output fluctuations with $\omega = 0.4$ and $\lambda_z = 3.0$ in the (s, n, z) coordinate system which is locally aligned with the streamlines of the base flow $(\bar{u}_s, 0, 0)$; see figure 3 for an illustration. Note that in this coordinate system $\bar{u}_s \geq 0$. As discussed in Finnigan (1983); Patel & Sotiropoulos (1997); Dwivedi *et al.* (2019), this coordinate system is convenient for the analysis of separated boundary layers especially within the recirculation region.

The streamwise specific kinetic energy $\mathcal{E}_s := u'_s u'_s$ obeys the transport equation,

$$\frac{\partial \mathcal{E}_s}{\partial t} + \bar{u}_s \frac{\partial \mathcal{E}_s}{\partial s} = \mathcal{P} + \mathcal{S} + \mathcal{V} + \mathcal{C} + \mathcal{F}, \quad (3.10)$$

where \mathcal{P} , \mathcal{S} , \mathcal{V} , and \mathcal{C} are the production, source, viscous, and curvature terms (see appendix B), and \mathcal{F} is the work done by external disturbances (Dwivedi *et al.* 2019,

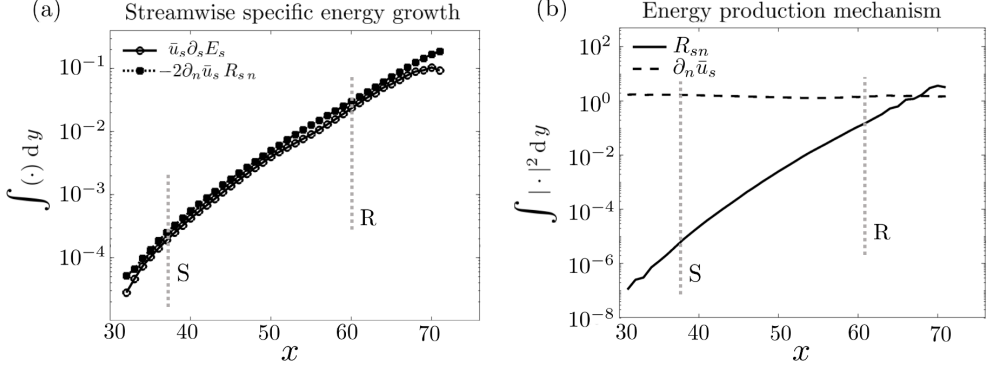


FIGURE 6. Streamwise variation of (a) $\bar{u}_s \partial_s E_s$ along with the dominant production term in equation (3.11a); (b) average fluctuation shear stress R_{sn} and base flow shear $\partial_n \bar{u}_s$.

appendix C). The production term \mathcal{P} quantifies interactions of fluctuation stresses with the base flow gradients, the source term \mathcal{S} corresponds to the perturbation component of the inviscid material derivative, the viscous term \mathcal{V} determines dissipation of kinetic energy by viscous stresses, and \mathcal{C} accounts for the curvature that arises from a coordinate transformation. While the dissipative viscous term \mathcal{V} is negative throughout the domain the production term \mathcal{P} is sign-indefinite, \mathcal{S} and \mathcal{C} are negligible, and \mathcal{F} is zero downstream of the forcing plane.

Insight into physical mechanisms can be gained by the analysis of dominant production terms in (3.10). Averaging over the time period $T = 2\pi/\omega$ and the spanwise wavelength λ_z of oblique fluctuations, $\langle \cdot \rangle := (T\lambda_z)^{-1} \int_0^T \int_0^{\lambda_z} (\cdot) dz dt$, and neglecting the terms that do not contribute significantly to the production of the averaged streamwise specific kinetic energy $E_s := \langle \mathcal{E}_s \rangle$ yields the following approximation to transport equation (3.10),

$$\bar{u}_s \frac{\partial E_s}{\partial s} + 2(\partial_s \bar{u}_s)E_s \approx -2(\partial_n \bar{u}_s)R_{sn}, \quad (3.11a)$$

where $R_{sn} := \langle u'_s u'_n \rangle$ denotes the averaged shear stress of the streamwise velocity fluctuations. The second term on the left-hand-side represents the production of fluctuations' energy that arises from the streamwise gradient of the base flow $\partial_s \bar{u}_s$ and the term on the right-hand-side determines the production term that originates from interactions of the base flow shear $\partial_n \bar{u}_s$ with the fluctuation shear stress R_{sn} .

In figure 6(a), we compare $\bar{u}_s \partial_s E_s := \bar{u}_s \partial E_s / \partial s$ with the dominant production term in (3.11a) to illustrate that $(\partial_n \bar{u}_s)R_{sn}$ dictates the streamwise growth of E_s . Figure 6(b) shows that the base shear $\partial_n \bar{u}_s$ remains almost constant throughout the shear layer. Thus, the streamwise growth of E_s shown in figure 6(a) primarily arises from the growth of the fluctuation shear stress R_{sn} whose streamwise transport we investigate next.

Since the production \mathcal{P} and curvature \mathcal{C} terms contribute most to the streamwise transport of R_{sn} for fluctuations with $\omega = 0.4$ and $\lambda_z = 3.0$, omitting negligible terms leads to the following approximate transport equation for R_{sn} (see appendix C),

$$\bar{u}_s \frac{\partial R_{sn}}{\partial s} + (\partial_s \bar{u}_s + K_s)R_{sn} \approx 2K_c E_s,$$

where K_c and K_s denote contributions that arise from the curvature normal to the streamlines and from deceleration along the streamline direction, respectively. In the (s, n, z) coordinate system, we have $K_c = -(\Omega + \partial_n \bar{u}_s)$, where $\Omega = \partial_x \bar{v} - \partial_y \bar{u}$ is the

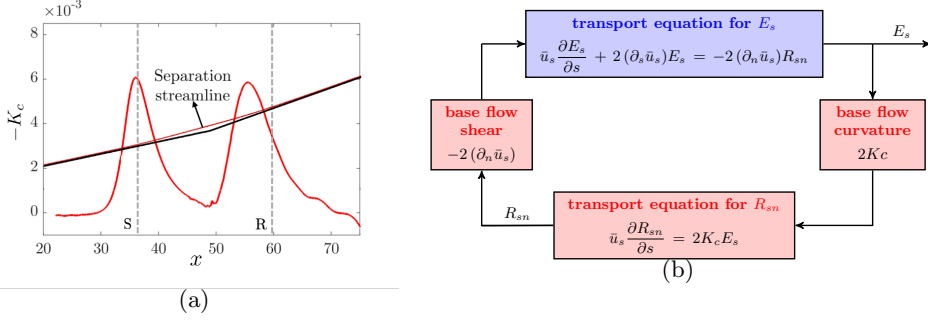


FIGURE 7. (a) Curvature ($-K_c$) of the laminar base flow along the separation streamline; (b) illustration of a physical mechanism that facilitates growth of the averaged streamwise specific kinetic energy E_s of oblique fluctuations in the separated shear layer.

vorticity of the base flow in the Cartesian coordinates (Finnigan 1983). Furthermore, since $K_s = -\partial_s \bar{u}_s$, the previous equation simplifies to

$$\bar{u}_s \frac{\partial R_{sn}}{\partial s} \approx 2K_c E_s. \quad (3.11b)$$

Equations (3.11a) and (3.11b) determine a coupled system of linear equations that governs the streamwise transport of E_s and R_{sn} in the separation zone for oblique fluctuations with $\omega = 0.4$ and $\lambda_z = 3.0$. The presence of flow separation leads to concave flow curvature $K_c < 0$ in the separated shear layer; figure 7(a) shows this negative curvature along the separation streamline and figure 7(b) illustrates the physical mechanism which is absent in attached boundary layers because of negligibly small positive streamwise curvature.

Concave base flow curvature (i.e., $K_c < 0$) and streamwise deceleration of the laminar base flow (i.e., $\partial_s \bar{u}_s < 0$) in the shear layer provide destabilizing effects in system (3.11). A simple mass-spring-damper analogy can be used to illustrate these destabilizing influences. Since the base shear $\partial_n \bar{u}_s$ remains almost constant throughout the shear layer (cf. figure 6(b)), its streamwise derivative can be neglected. Thus, differentiation of equation (3.11a) with respect to s , multiplication with \bar{u}_s , and substitution of (3.11b) into the resulting equation yield,

$$\bar{u}_s^2 \frac{\partial^2 E_s}{\partial s^2} + 3\bar{u}_s (\partial_s \bar{u}_s) \frac{\partial E_s}{\partial s} + 2(\bar{u}_s (\partial_{ss} \bar{u}_s) + 2K_c (\partial_n \bar{u}_s)) E_s \approx 0. \quad (3.12)$$

This linear differential equation with s -dependent coefficients governs the evolution of E_s for oblique fluctuations with $\omega = 0.4$ and $\lambda_z = 3.0$ in the separated shear layer. Figure 8(a) shows the streamwise evolution of the wall-normal integral of E_s along with the spatial variation of E_s near reattachment. In the regions where $K_c < 0$, the “spring constant” in this equation (i.e., $\bar{u}_s (\partial_{ss} \bar{u}_s) + 2K_c (\partial_n \bar{u}_s)$) can become negative; similarly, in the regions where the base flow experiences streamwise deceleration (i.e., $\partial_s \bar{u}_s < 0$), the “damping coefficient” in (3.12) becomes negative. As shown in figure 8(b), concave base flow curvature provides destabilizing influence throughout the separated shear layer and the growth of E_s is further enhanced by negative “damping coefficient” in the vicinity of the separation and reattachment locations.

In summary, input-output analysis identifies the spatial structure of oblique perturbations that amplify rapidly in the separation zone. Furthermore, by conducting transport analysis of the most energetic flow fluctuations, we have demonstrated that the resulting amplification arises from the curvature of the separated/reattaching base flow.

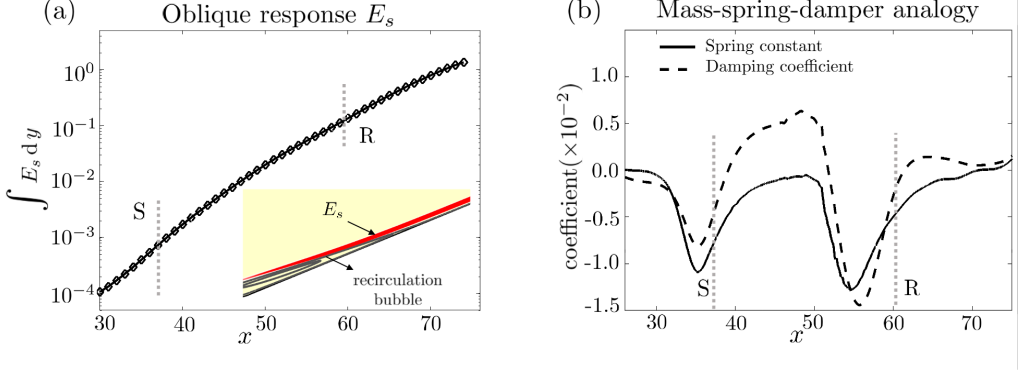


FIGURE 8. (a) Streamwise evolution of the wall-normal integral of $E_s := \langle u'_s u'_s \rangle$ for the primary output mode of oblique fluctuations with $(\omega = 0.4, \lambda_z = 3.0)$ along with contours of E_s in separated shear layer near reattachment (inset); (b) “spring constant” $2(\bar{u}_s(\partial_{ss}\bar{u}_s) + 2K_c(\partial_n\bar{u}_s))$ and “damping coefficient” $3\bar{u}_s(\partial_s\bar{u}_s)$ in equation (3.12).

4. Nonlinear interactions of oblique waves

In § 3, we used input-output analysis to identify oblique waves as the most energetic responses of the linearized flow equations in the presence of unsteady disturbances. Recent numerical simulations (Lugrin *et al.* 2021) show that, even in the presence of unsteady disturbances, the dominant response near the reattachment appears in the form of streamwise streaks. To investigate the origin of steady streaks in the presence of unsteady external disturbances we utilize a weakly nonlinear formulation based on a perturbation expansion in the amplitude of the oblique disturbances. While previous numerical studies of transition induced by oblique waves in low-speed channel (Schmid & Henningson 1992) and boundary layer (Chang & Malik 1994; Berlin & Henningson 1999; Mayer *et al.* 2011) flows show that nonlinear interactions of oblique waves generate streaks, we focus on the origin and spatial growth of these streaks in separated high-speed compressible boundary layer flows.

4.1. Weakly nonlinear analysis

In the presence of a small external disturbance,

$$\mathbf{d}(x, y, z, t) = \epsilon(\mathbf{d}_+(x, y)e^{i\omega t} + \mathbf{d}_-(x, y)e^{-i\omega t})e^{i\beta z}, \quad (4.1)$$

a weakly nonlinear analysis can be utilized to represent the flow state as

$$\mathbf{U}(\mathbf{x}, t) = \mathbf{U}^{(0)}(x, y) + \epsilon(\mathbf{U}_+^{(1)}(x, y)e^{i\omega t} + \mathbf{U}_-^{(1)}(x, y)e^{-i\omega t})e^{i\beta z} + \epsilon^2\mathbf{U}^{(2)}(\mathbf{x}, t) + \mathcal{O}(\epsilon^3), \quad (4.2)$$

where $\mathbf{d}_\pm^{(1)}$ and $\mathbf{U}_\pm^{(1)}$ are the principal oblique input-output pairs resulting from the linearized analysis in § 3. At $\mathcal{O}(\epsilon^2)$, the fluctuation’s dynamics are governed by

$$\left[\frac{\partial}{\partial t} - \mathcal{A}(\mathbf{U}^{(0)}) \right] \mathbf{U}^{(2)} = \mathcal{N}^{(2)}, \quad (4.3)$$

where $\mathcal{A}(\mathbf{U}^{(0)})$ denotes the compressible NS operator resulting from linearization around the base flow $\mathbf{U}^{(0)}$ and $\mathcal{N}^{(2)}$ is the nonlinear term that accounts for quadratic interactions between $\mathbf{U}_+^{(1)}$ and $\mathbf{U}_-^{(1)}$; see appendix D for details. Furthermore, the quadratic nature

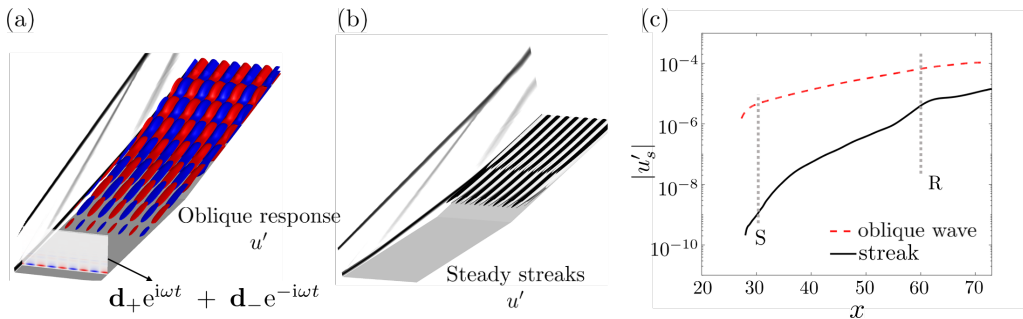


FIGURE 9. (a) Setup for weakly nonlinear analysis: a pair of dominant input modes with $(\omega = \pm 0.4, \lambda_z = 3)$ resulting from input-output analysis is introduced at $x_{\text{in}} = 25$ and the corresponding streamwise velocity fluctuations arise as the output of the linearized dynamics. (b) Steady streamwise streaks with $\lambda_z = 1.5$ are triggered by weakly nonlinear interactions of oblique waves. (c) Streamwise velocity fluctuations corresponding to the steady streaks resulting from weakly nonlinear analysis and the envelope of the corresponding oblique fluctuations along the base flow separation streamline.

of the nonlinear term allows us to express $\mathbf{U}^{(2)}(\mathbf{x}, t)$ as,

$$\mathbf{U}^{(2)}(\mathbf{x}, t) = \left(\mathbf{U}_{\text{streak}}^{(2)}(x, y) + \mathbf{U}_+^{(2)}(x, y)e^{2i\omega t} + \mathbf{U}_-^{(2)}(x, y)e^{-2i\omega t} \right) e^{2i\beta z} \quad (4.4)$$

where the steady component of the response at $\mathcal{O}(\epsilon^2)$ satisfies

$$\left[\mathcal{A} \left(\mathbf{U}^{(0)} \right) \mathbf{U}_{\text{streak}}^{(2)} \right] (x, y) = -\mathcal{N}_{\text{streak}}^{(2)}(x, y), \quad (4.5)$$

Finally, the finite-volume discretization of (4.5) yields,

$$\mathbf{A} \mathbf{q}_{\text{streak}}^{(2)} = -\mathbf{N}_{\text{streak}}^{(2)}, \quad (4.6)$$

where \mathbf{A} is the dynamical generator in the linearized state-space model (3.4). Thus, the resolvent associated with (3.4) evaluated at $\omega = 0$ maps the forcing $\mathbf{N}_{\text{streak}}^{(2)}$ that arises from quadratic interactions of small oblique waves and yields steady streamwise streaks,

$$\mathbf{q}_{\text{streak}}^{(2)} = \mathbf{R}(i0) \mathbf{N}_{\text{streak}}^{(2)} = -\mathbf{A}^{-1} \mathbf{N}_{\text{streak}}^{(2)}. \quad (4.7)$$

To investigate the emergence of streaks from unsteady disturbances, we evaluate weakly nonlinear evolution of the oblique waves which undergo largest amplification by the linearized dynamics at the reattachment (i.e., at $x = 60$). In particular, we introduce forcing inputs with $(\omega = \pm 0.4, \lambda_z = 3)$ that are identified via input-output analysis in § 3.

Figure 9(a) illustrates the setup in which a pair of input modes with $(\omega = \pm 0.4, \lambda_z = 3)$ is introduced at $x_{\text{in}} = 25$. The resulting response at $\mathcal{O}(\epsilon)$ is given by oblique waves with opposite phase velocities, leading to a checkerboard wave pattern in the spanwise direction. The oblique fluctuations undergo rapid amplification in the separation zone as they convect downstream. Figure 9(b) shows steady streamwise velocity fluctuations at $\mathcal{O}(\epsilon^2)$ that arise from weakly nonlinear interactions of oblique waves with $\pm\omega$. The steady response is given by streamwise streaks with half the spanwise wavelength $\lambda_z^{\text{streaks}} = \lambda_z^{\text{oblique}}/2 = 1.5$ of the forcing input. These streaks experience significant amplification in the reattachment zone, as illustrated in figure 9(c) which shows spatial evolution of the streamwise velocity perturbations u'_s . For comparison, the envelope of u'_s associated with the corresponding oblique fluctuations is also plotted. As oblique waves grow through the

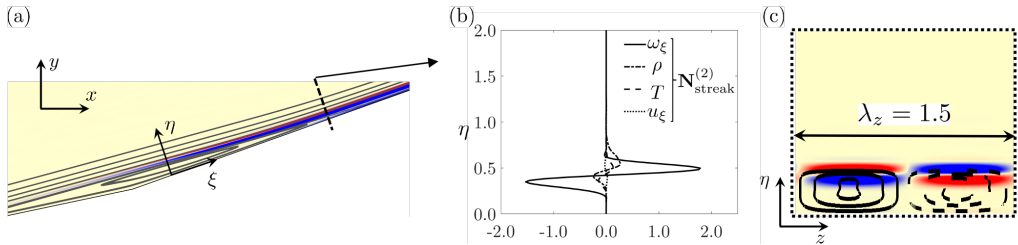


FIGURE 10. (a) Real part of the streamwise vorticity forcing component that arises from weakly nonlinear interactions of oblique waves $\mathbf{N}_{\text{streak}}^{(2)}$ in the (x, y) plane along with the base flow streamlines. (b) Wall-normal profiles of the forcing terms to the streamwise vorticity, density, temperature, and streamwise velocity equations that originate from $\mathbf{N}_{\text{streak}}^{(2)}$ before reattachment, at $x = 58$. (c) Spatial structure of the forcing near reattachment in the (z, η) plane (color plots) along with the resulting streak response u'_s (contour lines) at $x = 58$.

shear layer, the streaks experience much higher amplification and their spatial growth peaks near the reattachment point.

A weakly nonlinear analysis allowed us to demonstrate that the source of steady streaks at $\mathcal{O}(\epsilon^2)$ arises from quadratic interactions of $\mathcal{O}(\epsilon)$ oblique waves. Figure 10(a) utilizes a wall-aligned (ξ, η) coordinate system to illustrate a forcing term $\mathbf{N}_{\text{streak}}^{(2)}$ in (4.5). We recall that ξ and η denote the directions parallel and normal to the wall, respectively. Large amplification of oblique waves that result from linearized analysis in the reattachment region triggers strongest forcing $\mathbf{N}_{\text{streak}}^{(2)}$ in that region. Figure 10(b) shows the wall-normal profiles of the forcing term to the mass, momentum, and temperature equations in (4.3) before reattachment at $x = 58$. We observe the strongest contribution of the forcing to the wall-normal and spanwise components of the momentum equations, thereby demonstrating its vortical nature. Figure 10(c) illustrates the spatial structure of the forcing near reattachment in the (z, η) plane. The forcing term $\mathbf{N}_{\text{streak}}^{(2)}$ which forms counter-rotating vortices in the separated shear layer is 90° out of phase relative to the induced streak response u'_s . In contrast to the dominant vortical forcing resulting from the linearized analysis, the vortical source term that arises from weakly nonlinear interactions of oblique waves primarily lies downstream of recirculation zone.

4.2. Direct numerical simulations

Weakly nonlinear analysis shows that the steady streamwise streaks are triggered by a vortical forcing that arises from quadratic interactions of spatially growing unsteady oblique waves. Herein, we utilize direct numerical simulations (DNS) to examine validity of a weakly nonlinear approximation in the presence of unsteady external disturbances.

In DNS, we place the inflow boundary at $x = 20$ and, at this location, we interpolate the inflow profile that results from 2D base flow computations. To avoid spurious numerical errors we utilize a non-reflecting numerical sponge near the outflow. A 3D grid with uniform spacing in the spanwise direction is used in our simulations. The grid resolution in the (x, y) plane is the same as the one used in steady 2D base flow calculations. We apply periodic boundary conditions in the spanwise direction and choose 16 grid points per spanwise wavelength of the disturbance (this is achieved with $\Delta z \approx 0.19$). We use low-dissipation sixth-order spatially accurate kinetic-energy-consistent (KEC) fluxes (Subbareddy & Candler 2009) and the explicit third-order Runge-Kutta scheme with CFL number 0.5 to carry out time integration in the US3D hypersonic flow solver. The low-dissipation KEC fluxes were previously employed in high-

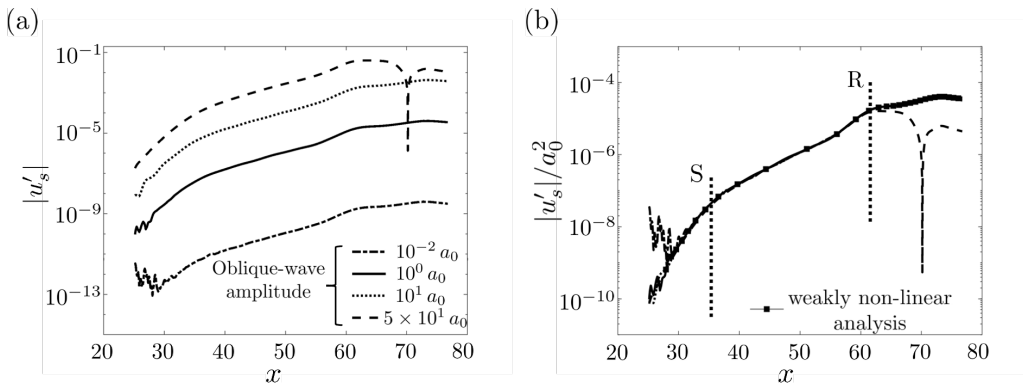


FIGURE 11. (a) Streamwise velocity fluctuations u'_s along the separation streamline associated with the steady streaks at $\lambda_z = 1.5$; DNS results for various amplitudes of oblique disturbances with $(\omega = \pm 0.4, \lambda_z = 3)$ are shown. (b) DNS results normalized with the square of the amplitude a_0 of oblique disturbances are compared with the results of weakly nonlinear analysis.

fidelity simulations of transitional and turbulent hypersonic boundary layers (Subbareddy *et al.* 2014; Subbareddy & Candler 2012).

The unsteady disturbances are introduced as volumetric sources of excitation. To verify that the streaks result from a quadratic interaction of oblique waves (with $\omega = \pm 0.4$), we evaluate the spatial evolution of the steady streamwise velocity perturbations u'_s resulting from the unsteady input modes of various amplitudes in figure 11. The reference amplitude $a_0 = 3.1 \times 10^{-7} \rho_\infty U_\infty \omega$ is chosen such that the largest value of the non-dimensional disturbance momentum is normalized to one. As shown in figure 11(a), streaks triggered by unsteady oblique disturbances undergo similar spatial growth across the range of forcing amplitudes. Figure 11(b) demonstrates that the magnitude of streamwise velocity fluctuations collapses when scaled with a_0^2 . This demonstrates an excellent agreement between streak profiles resulting from DNS and a weakly nonlinear analysis (that leads to equation (4.5)). Deviations from predictions of the weakly nonlinear analysis are only observed for the largest amplitude considered and they are manifested by saturation of streaks in post-reattachment region.

Collapse of spatial profiles that characterize amplification of streaks irrespective of the amplitude of oblique disturbances, which differ by $\mathcal{O}(10^4)$, shows that streaks generated via quadratic interactions of oblique waves undergo linear amplification in the separation zone. This demonstrates predictive power of the weakly nonlinear analysis across the range of forcing amplitudes. In what follows, we utilize input-output analysis to characterize evolution of streaks and uncover corresponding amplification mechanisms.

4.3. Representation of streaks in terms of output resolvent modes

As described in § 3.1, the left and right singular vectors of the frequency response provide orthonormal bases of input and output spaces that can be used to study responses of the double-wedge flow to external excitations. In particular, the streaks resulting from weakly nonlinear interactions of oblique waves (cf. equation (4.7)) can be represented using SVD of the resolvent associated with the linearized system (3.4) at $\omega = 0$,

$$\mathbf{q}_{\text{streak}}^{(2)} = \mathbf{R}(\mathbf{i}0) \mathbf{N}_{\text{streak}}^{(2)} = \sum_i \sigma_i \phi_i \langle \mathbf{d}_i, \mathbf{N}_{\text{streak}}^{(2)} \rangle_E. \quad (4.8)$$

Here, σ_i is the i th singular value and (\mathbf{d}_i, ϕ_i) are the corresponding input-output modes of the resolvent $\mathbf{R}(\mathbf{i}0) = -\mathbf{A}^{-1}$. For $\lambda_z = 1.5$, the inner product $\langle \cdot, \cdot \rangle_E$ is carried over the

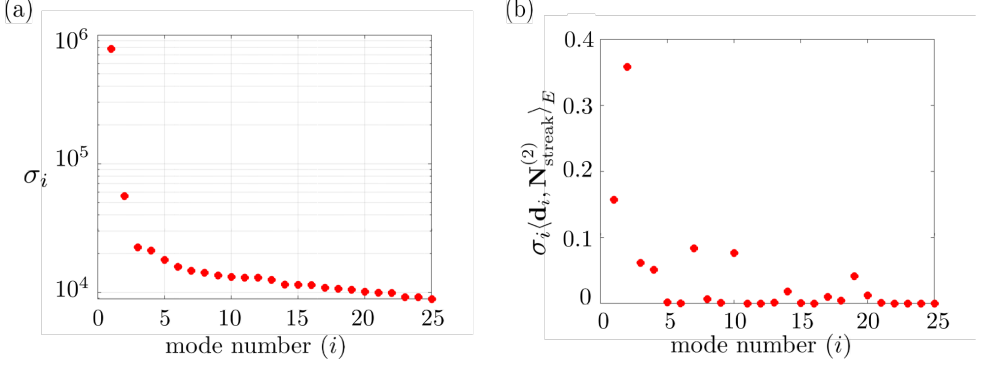


FIGURE 12. (a) Singular values of the resolvent associated with the dynamics linearized around the 2D laminar flow evaluated at $(\omega, \lambda_z) = (0, 1.5)$. (b) Contribution of the i th output mode ϕ_i to steady streaks that are triggered by weakly nonlinear interactions of oblique waves.

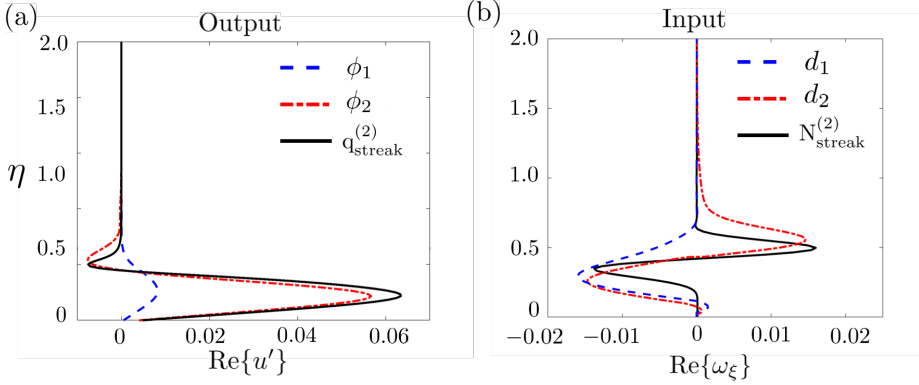


FIGURE 13. The wall-normal profiles of the real part of streamwise velocity fluctuations corresponding to (a) streaks resulting from weakly nonlinear analysis and the first two output modes after reattachment, at $x = 65$; (b) vortical forcing resulting from weakly nonlinear interactions of oblique waves and the first two input modes in reattaching shear layer, at $x = 57$.

entire flow domain in (x, y) and the product between σ_i and the projection coefficient $\langle \mathbf{d}_i, \mathbf{N}_{\text{streak}}^{(2)} \rangle_E$ quantifies the contribution of the i th output mode ϕ_i to steady streaks that are triggered by weakly nonlinear interactions of oblique waves.

Figure 12(a) shows 25 largest singular values of the resolvent for the linearized system (3.4) with $(\omega = 0, \lambda_z = 1.5)$. Even though the principal singular value σ_1 is an order of magnitude larger than σ_2 , figure 12(b) demonstrates that the second output mode ϕ_2 contributes most to $\mathbf{q}_{\text{streak}}^{(2)}$. Figure 13(a) shows the wall-normal profiles of the streamwise velocity component u' associated with $\mathbf{q}_{\text{streak}}^{(2)}$ and the first two output modes (ϕ_1, ϕ_2) of the resolvent. We observe striking similarity between streaks generated by weakly nonlinear interactions of oblique waves and the second output mode in the post-reattachment region, at $x = 65$. Similarly, figure 13(b) compares the wall-normal shapes of the corresponding input modes \mathbf{d}_1 and \mathbf{d}_2 with the forcing $\mathbf{N}_{\text{streak}}^{(2)}$ that arises from quadratic interactions. The input modes are visualized in the reattaching shear layer, at $x = 57$, and the streamwise vorticity component of \mathbf{d}_2 provides a good approximation to the vortical forcing that captures interactions of unsteady oblique fluctuations.

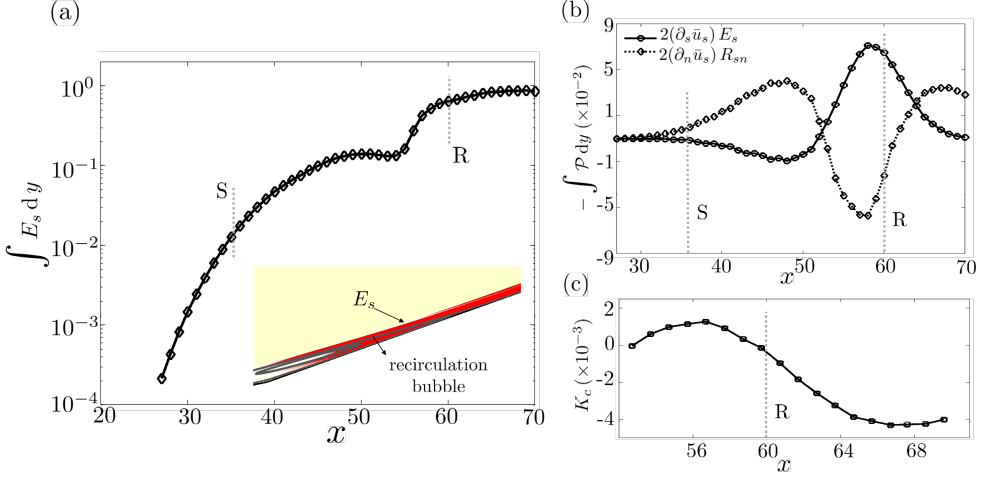


FIGURE 14. (a) Streamwise evolution of the wall-normal integral of $E_s = \langle u'_s u'_s \rangle$ for the second output mode associated with streaks at $(\omega = 0, \lambda_z = 1.5)$ along with contours of E_s near reattachment (inset); (b) streamwise variation of deceleration and shear components of the spanwise averaged production term $\langle \mathcal{P} \rangle$ in the transport equation for E_s ; and (c) base flow curvature K_c near reattachment.

4.4. Amplification of streaks: physical mechanism

As demonstrated above, near reattachment, the streaks triggered by weakly nonlinear interaction of oblique waves are well approximated by the second output mode of the resolvent associated with the linearized equations at $(\omega = 0, \lambda_z = 1.5)$. To gain insight into the amplification mechanism that generates steady streaks, we examine the dominant terms in the energy transport equation for this output mode. Similar to the analysis in § 3.3, we utilize the (s, n, z) coordinate system which is locally aligned with the streamlines of the base flow $(\bar{u}_s, 0, 0)$. The transport of the spanwise averaged specific kinetic energy of streamwise velocity fluctuations $E_s = \langle u'_s u'_s \rangle$ and fluctuation shear stress $R_{sn} = \langle u'_s u'_n \rangle$ of the second output mode is approximately governed by equations (3.11a) and (3.11b) in § 3.3, where $\langle \cdot \rangle$ denotes spanwise averaging.

Figure 14(a) shows the streamwise evolution of the wall-normal integral of E_s for the second output mode associated with streaks at $(\omega = 0, \lambda_z = 1.5)$. In contrast to the oblique waves (cf. figure 8(a)), we observe a non-monotonic x -dependence of E_s within the separation zone. Furthermore, near reattachment streaks are mostly present inside the recirculation bubble and, to gain additional insight, we evaluate contributions of the production terms in (3.11a). Figure 14(b) shows that both streamwise deceleration and shear components of the production term contribute to amplification of streaks in different regions of the separated laminar flow. Within the bubble the effect of perturbation shear stresses is counteracted by the base flow acceleration (i.e., $\partial_s \bar{u}_s > 0$). Further downstream near reattachment, the base flow curvature K_c is positive (cf. figure 14(c)) and the streamwise deceleration term dominates. This is in concert with the analysis of the contribution of the first (i.e., most amplified) output mode to the amplification of streaks in a compression ramp flow (Dwivedi *et al.* 2019), which also revealed dominance of streamwise deceleration near reattachment. On the other hand, in the post-reattachment region, the shear term contributes most to the amplification of streaks via concave streamline curvature (i.e. $K_c < 0$).

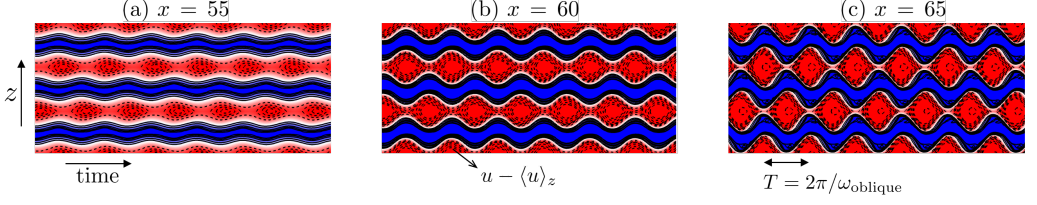


FIGURE 15. Streamwise streaks in the plane close to the wall, $\eta = 0.25$, at three different streamwise locations: (a) before reattachment, at $x = 55$; (b) at reattachment, at $x = 60$; and (c) after reattachment, at $x = 65$. The low-speed streaks are marked in blue color (solid lines) and high-speed streaks are marked in red color (dashed lines).

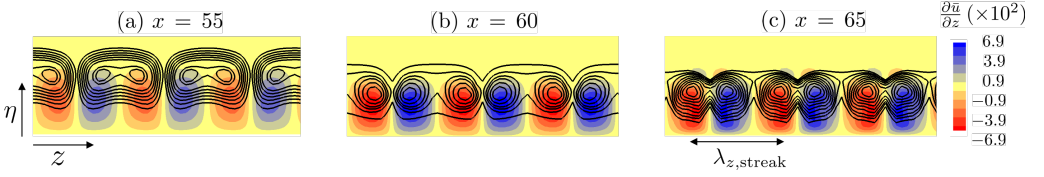


FIGURE 16. Color plots of the spanwise gradient of time-averaged streamwise velocity $\partial \bar{u} / \partial z$ and contour lines of u'_{rms} at the same streamwise locations as in figure 15.

5. Secondary instabilities and breakdown

The weakly nonlinear analysis demonstrates that small unsteady disturbances induce steady 3D streaks in a hypersonic flow over a double-wedge. These streaks result from quadratic interactions of oblique waves and they undergo rapid amplification primarily because of streamwise deceleration near reattachment. Downstream of reattachment, the streaks grow large enough to modify the time-averaged 2D flow. In this section, we utilize DNS to examine breakdown of streaks caused by their interactions with incoming oblique waves and describe instantaneous and statistical properties of the transitioning flow field.

To study the onset of transition, we extend computational domain in the streamwise direction downstream of reattachment. Computational domain of size $80 \times 13 \times 9$ in the streamwise, wall-normal, and spanwise directions is discretized using $900 \times 249 \times 192$ grid points (i.e., 43 million cells). The grid is constructed to ensure uniform spacing in the streamwise and spanwise directions and, in the wall-normal direction, the mesh is stretched to ensure $y^+ < 0.3$ at the wall. This resolution is similar to the ones used in previous DNS studies of spatially evolving compressible transitional (Mayer *et al.* 2011; Franko & Lele 2013) and turbulent boundary layers (Duan *et al.* 2011). Furthermore, as we demonstrate below, statistical quantities obtained post-breakdown are in accordance with well-established correlations of fully turbulent compressible boundary layers. We use input modes with $(\omega = \pm 0.4, \lambda_z = 3)$, identified by the linearized analysis, as an exogenous disturbance to drive the flow in DNS. The disturbance amplitude is set to $A^{ob} = 1.5 \times 10^{-5} \rho_\infty U_\infty \omega = 50a_0$ and is determined based on the results reported in figure 11. With this amplitude, fluctuations grow linearly in the recirculation region but saturate nonlinearly post-reattachment (i.e., beyond $x = 60$).

In figure 15, we show time evolution of streaks in the plane close to the wall, at $\eta = 0.25$, for three different values of x . These plots demonstrate that, in the presence of unsteady oblique disturbances, the steady streaks undergo spanwise motion close to reattachment. The identified spanwise oscillations become stronger as we progress downstream and their period corresponds to the time period of oblique wave inputs. We note the presence of

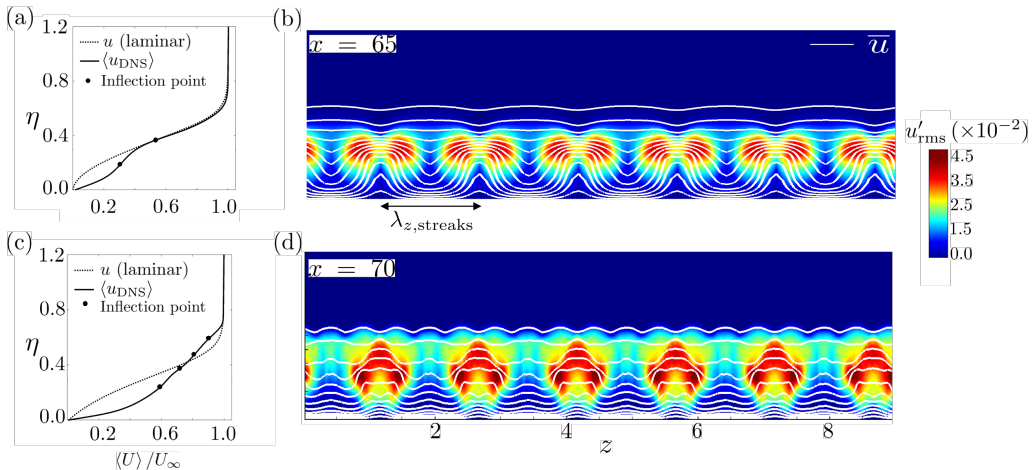


FIGURE 17. (a) Wall-normal profiles of laminar and mean streamwise velocity components at $x = 70$. (b) Color plots of u'_{rms} along with contour lines of time-averaged streamwise velocity.

a “sinuous-subharmonic” motion, where two adjacent low-speed streaks oscillate out of phase, and observe that the amplitude of spanwise oscillations almost doubles as we move from $x = 55$ to $x = 65$.

In figure 16, we illustrate the effect of streak oscillations on the mean flow by visualizing the root-mean-square of temporal fluctuations in the streamwise velocity. At different streamwise locations, fluctuations are plotted against $\partial \bar{u} / \partial z$, which characterizes steady spanwise variations of the mean flow. Initially, unsteadiness is restricted to the oblique wave pair, which is located further away from the wall relative to streaks. However, at $x = 65$, unsteadiness is observed in the region of the largest spanwise shear because of the presence of streaks. This “locking-in” of u'_{rms} with streak oscillations identifies late stages of the streak evolution just before smaller-scales (associated with higher frequencies) set in.

Amplification of streaks and their unsteadiness induce rapid steepening of spanwise and wall-normal mean flow gradients, thereby leading to the emergence of inflection points in the mean (time- and spanwise-averaged) flow. Figure 17(a) shows the resulting inflectional mean flow profile and figure 17(b) shows the location of unsteady fluctuations with respect to the streaks. As we move from $x = 65$ to $x = 70$, we note the appearance of higher spanwise wavenumbers in the streaks as well as in the unsteady fluctuations. As discussed by Hall & Horseman (1991); Yu & Liu (1994), inflectional points in the mean velocity serve as an indicator of its susceptibility to the growth of broadband fluctuations. Amplification of high-frequency harmonics is also observed in the temporal spectra of the fluctuations. Therefore, at $x = 70$, flow is well within fully nonlinear stages of transition. We also note strong spatial correlation of unsteady fluctuations with the spanwise shear associated with the streaks, even at this nonlinear stage.

In figure 18, we plot Q -isosurfaces of the instantaneous flow-field. These visualize vortical structures that arise from sinuous-subharmonic motion of the streaks, prior to breakdown of the flow. We note the appearance of staggered lambda vortices, similar to the ones identified in transition induced by oblique waves in incompressible boundary layers (Berlin *et al.* 1999). These vortical structures are also sometimes referred to as X -vortices, for reasons illustrated in the (η, z) slice array plot in figure 18. Initially, at $x \approx 62$, we observe that the interaction with the oblique waves causes the roll-up of the low-speed streak as they come together due to sinuous-subharmonic motion.

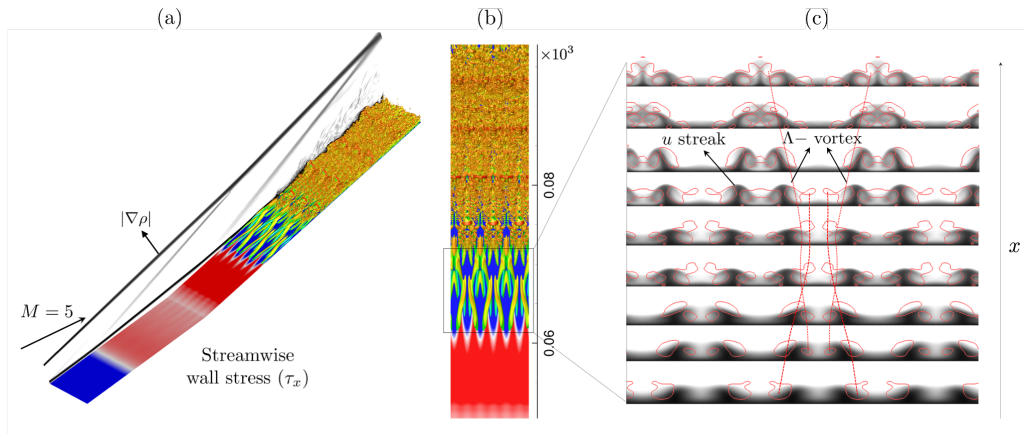


FIGURE 18. (a) Instantaneous isosurface of the Q -criterion colored by contours of the streamwise velocity; (b) contour plot of the wall-shear stress show the formation of streaks before transition; and (c) (η, z) slices of instantaneous streamwise velocity contours along with contour lines of the Q -criteria.

Further downstream, as the flow structures associated with the X -vortices spread apart, we see that upward jets of low-speed flow form mushroom structures. As these low-speed regions oscillate further, they interact to generate fluctuations with higher spanwise wavenumbers. Finally, at $x \approx 70$, the shear introduced by the upward jets of low-speed streaks becomes significant enough to cause a local Kelvin-Helmholtz instability that induces streamwise rollers (Reddy *et al.* 1998). At this stage, the laminar boundary layer flow has started to break down to turbulence.

6. Transition to turbulence

Our DNS study demonstrates that amplification of steady streaks, that result from quadratic interactions of oblique waves, leads to a formation of a 3D inflectional boundary layer profile. During this process, fluctuations with multiple spatial and temporal scales develop and flow eventually becomes turbulent. While a detailed description of the flat plate compressible turbulent boundary layers was provided in Duan *et al.* (2011); Pirozzoli & Bernardini (2011), we examine wall and boundary layer statistics in the transition zone on the second wedge following the appearance of the inflectional flow profile but before the development of fully developed turbulence.

6.1. Wall statistics

6.1.1. Skin friction

A boundary layer transition is characterized by a rapid increase in wall friction. Figure 19(a) utilizes instantaneous wall-shear distribution to identify transitional and turbulent regions. The wall-shear stress experiences sinuous-subharmonic modulation downstream of the reattachment (at $x = 60$, i.e., $Re_x = 8.2 \times 10^5$) and finer spanwise scales emerge downstream of the inflectional boundary layer profile after $x = 80$ (i.e., $Re_x \approx 11 \times 10^5$). As shown in figure 19(b), this location coincides with the highest value of time-averaged wall shear. Even though significant attenuation of spanwise variations of the wall-shear stress associated with the initial streaks takes place by $x = 80$, nonlinear interactions within the transition zone lead to the appearance of new streaks further downstream.

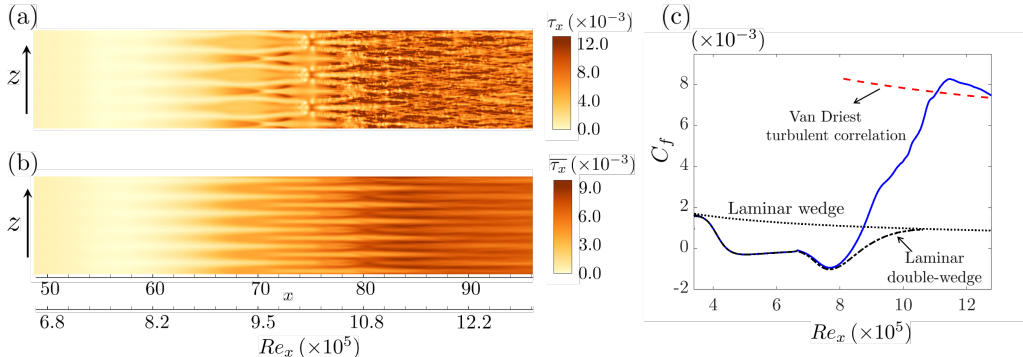


FIGURE 19. Streamwise variations of (a) instantaneous and (b) time-averaged streamwise shear stresses as well as (c) wall skin friction coefficient.

The spatial extent of transition zone is visualized in figure 19(c) by showing streamwise development of the wall skin friction coefficient,

$$C_f = \frac{1}{T} \frac{1}{L_z} \int_0^T \int_0^{L_z} \frac{\tau_w^*}{\frac{1}{2} \rho_e^* (U_e^*)^2} dz dt. \quad (6.1)$$

Here, τ_w^* is the dimensional shear stress at the wall, ρ_e^* and u_e^* are the dimensional density and streamwise velocity at the boundary layer edge, L_z is the spanwise extent of the computational domain, and $T = 4L_x/u_\infty^*$. The values of C_f in laminar flows over a 12 degree wedge and over the double-wedge are also plotted for comparison. The skin friction coefficient drops because of flow separation but it grows again after reattachment. Near and downstream of reattachment, we observe a significant difference between laminar and turbulent values of C_f . After $Re_x = 11.5 \times 10^5$, when C_f starts to decay with x , the wall-friction coefficient is about seven times larger than its laminar counterpart. A comparison with the Van-Driest turbulent correlation for standard compressible boundary layers demonstrates that the flow on the second wedge is approaching fully developed turbulent values towards the end of the computational domain.

6.1.2. Wall temperature

We next examine distribution of wall temperature in the transition zone. In flows with adiabatic walls, there is no heat transfer to the wall and viscous dissipation near the wall converts kinetic into internal energy. This leads to high temperatures near the wall as well as in the associated thermal boundary layer and 3D patterns in the wall temperature are caused by temperature transport within the boundary layer by flow fluctuations.

Figures 20(a) and 20(b) illustrate instantaneous and mean wall temperatures in the transition zone. In contrast to the instantaneous skin friction, where the streaks determine the spanwise modulation prior to flow transition, the instantaneous wall temperature contains strong imprints of unsteady oblique waves. The role of the streaks and higher spanwise harmonics becomes apparent when we examine the time-averaged wall temperature.

In Figure 20(c), we illustrate the mean wall-temperature along the double-wedge. Even though temperature variations are not significant under present conditions, its analysis can be informative for different free-stream conditions. Comparison with the double wedge laminar solution shows that the wall temperature is higher in the 3D flow field immediately after the separation point and that it rises rapidly post-reattachment. In the transition zone, we observe an overshoot before reduction to its turbulent value.

Previous high-speed transition studies on isothermal walls have also observed heat

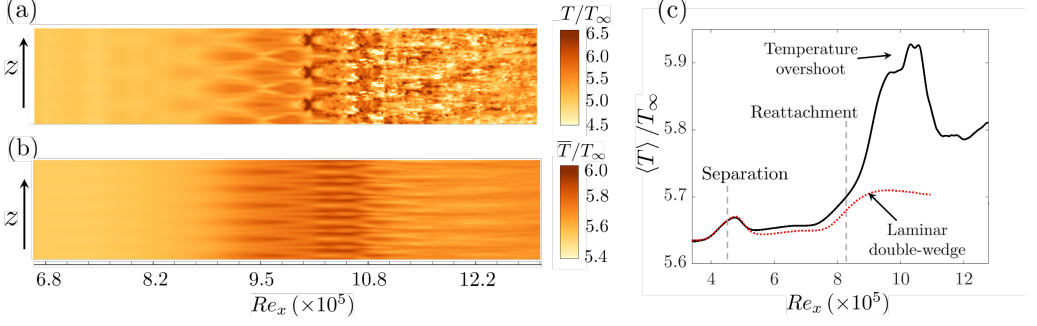


FIGURE 20. Streamwise variations of (a) instantaneous; (b) time-averaged; and (c) time- and spanwise-averaged wall temperatures.

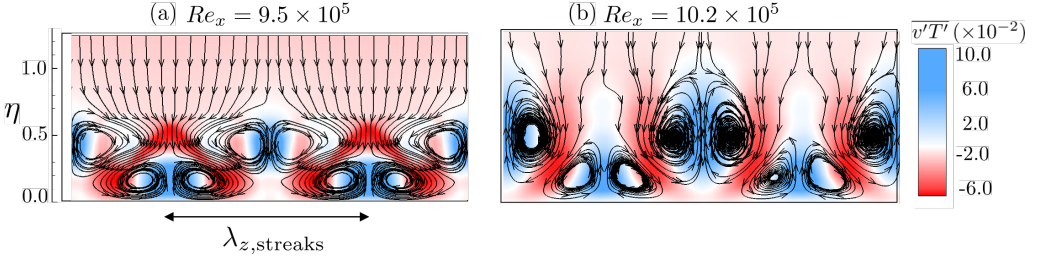


FIGURE 21. Contour lines of time-averaged wall-normal temperature flux $\overline{v'T'}$ at (a) $Re_x = 9.5 \times 10^5$ and (b) $Re_x = 10.2 \times 10^5$. The streamlines in the (z, η) plane are computed using the time-averaged wall-normal and spanwise velocity components.

flux overshoot (Franko & Lele 2013). For adiabatic walls, we investigate the temperature overshoot by examining perturbation temperature fluxes normal to the wall. Figure 21 shows the spanwise variation of $\langle v'T' \rangle$ prior to the overshoot (at $Re_x = 9.5 \times 10^5$) and near the overshoot (at $Re_x = 10.2 \times 10^5$). The streamlines are used to visualize the flow in the cross-stream (η, z) -plane at a given streamwise location and to highlight structure of the streaks. As shown in figure 21(a), the near-wall vortices become stronger before the overshoot and they can pull colder fluid to the wall. Furthermore, figure 21(b) illustrates that, close to the overshoot, nonlinear interactions weaken near-wall vortices while strengthening the outer vortices near the boundary layer edge. The outer vortices entrain more fluid and reduce transport of cold fluid to the wall, thereby causing higher wall temperatures. In the post-transition region, broadband turbulent fluctuations enhance mixing across the thermal boundary layer and the wall temperature drops relative to its values in the transitional zone.

6.2. Towards a turbulent compressible boundary layer

We next utilize data from our DNS to examine first- and second-order statistics as the boundary layer approaches fully turbulent regime and quantify changes caused by the emergence of multiple spatial and temporal scales in the latter stages of transition.

At a given streamwise location, we report statistics in terms of the inner coordinate η^+ which is obtained by non-dimensionalizing the wall-normal coordinate with the local viscous length δ_ν . Figure 22(a) shows the mean streamwise velocity u^+ non-dimensionalized by the local friction velocity u_τ . The mean profile is obtained by averaging in time over $2L_x/u_\infty$ and in the spanwise direction over the extent of the computational domain L_z .

In the presence of density variation along the compressible boundary layer, we utilize the Van-Driest transformation,

$$u_c(\eta) = \int_0^{\langle u \rangle} \sqrt{\frac{\langle \rho \rangle}{\langle \rho \rangle_w}} d\hat{u} = \int_0^\eta \sqrt{\frac{\langle \rho \rangle}{\langle \rho \rangle_w}} \frac{\partial \langle u \rangle}{\partial \hat{\eta}} d\hat{\eta}, \quad (6.2)$$

to compare the transitional velocity profiles with the ‘log-law’ observed in incompressible turbulent boundary layers (White & Majdalani 2006), where $\langle \cdot \rangle$ denotes averaging over time and spanwise direction, and $\langle \rho \rangle_w$ is the mean density at the wall. A fully developed turbulent boundary layer is characterized by the presence of the viscous sublayer close to the wall ($\eta^+ < 10$), where $u_c^+ = \eta^+$, and further away from the wall the mean velocity obeys the log-law,

$$u_c^+ = (1/\kappa) \ln(\eta^+) + C, \quad (6.3)$$

where $\kappa = 0.41$ and $C = 5.2$.

Figure 22(a) shows that the mean velocity in the boundary layer approaches the fully turbulent profile at $Re_x = 1.2 \times 10^6$. Upstream of this location, within the transition zone, the boundary layer has a significantly greater momentum and most of it lies away from the wall. Furthermore, closer to the wall, the slope of the streamwise velocity profile is larger than the slope obtained using viscous sublayer profile of a fully turbulent flow. This observation is consistent with the overshoot in skin-friction coefficient within the transition zone; cf. figure 19(b).

In addition to the mean velocity, the mean temperature profile plays an important role in heat transfer and material response analysis of hypersonic flows. Walz’s modified Crocco-Busemann relation,

$$\frac{\langle T \rangle}{\langle T_e \rangle} = \frac{\langle T_w \rangle}{\langle T_e \rangle} + \frac{\langle T_r \rangle - \langle T_w \rangle}{\langle T_e \rangle} \frac{\langle u \rangle}{\langle u_e \rangle} + \frac{\langle T_e \rangle - \langle T_r \rangle}{\langle T_e \rangle} \left(\frac{\langle u \rangle}{\langle u_e \rangle} \right)^2, \quad (6.4)$$

is commonly used to describe the relation between temperature and velocity in a zero pressure gradient turbulent boundary layer. Here, $\langle u_e \rangle$ and $\langle T_e \rangle$ denote the mean boundary layer edge velocity and temperature, respectively, $\langle T_r \rangle$ is the mean recovery temperature and, since the wall is adiabatic, the mean wall temperature is determined by $\langle T_w \rangle = \langle T_r \rangle$. In spite of pressure variations post-reattachment, figure 22(b) demonstrates that the quadratic relation in equation (6.4) holds throughout the transition zone. As the flow approaches a fully turbulent profile, we see a slight deviation from this relation in the outer region away from the wall; this observation is in agreement with prior studies of fully turbulent compressible boundary layers (Duan *et al.* 2011).

We next examine spatial development of flow fluctuations by evaluating second-order statistics and comparing them with those observed in a Mach 5 fully developed turbulent flat plate boundary layer (Duan *et al.* 2011). Figures 23(a)-(c) show the streamwise variation of the density-weighted root-mean-square (RMS) values of the streamwise, wall-normal, and spanwise velocity fluctuation components. In the transition zone, we observe large values of fluctuations away from the wall in all three plots. Further downstream, at $Re_x = 1.2 \times 10^6$, the RMS values closer to the wall are in agreement with fully turbulent values. However, away from the wall, the RMS values of u' and w' deviate from the flat plate profiles. We attribute this deviation to the presence of 3D oblique waves and streaks that persist downstream because of continuous upstream forcing in our setup.

To illustrate the broadband nature of velocity fluctuations in the later stages of transition, in figure 23(d) we evaluate the spanwise wavenumber dependence of the individual contributions of velocity fluctuations to the 1D energy spectrum at $Re_x =$

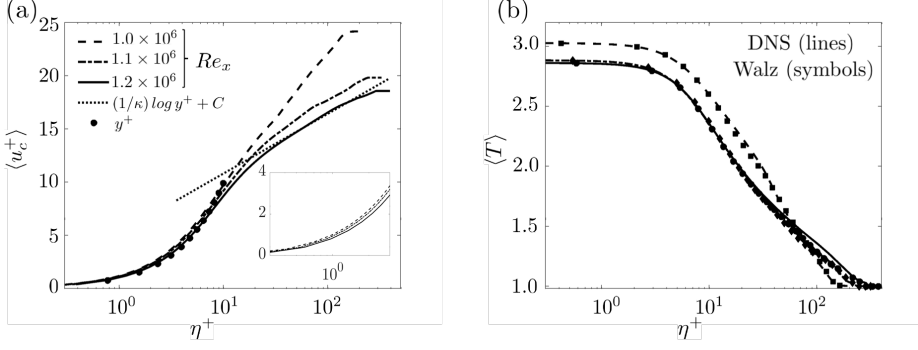
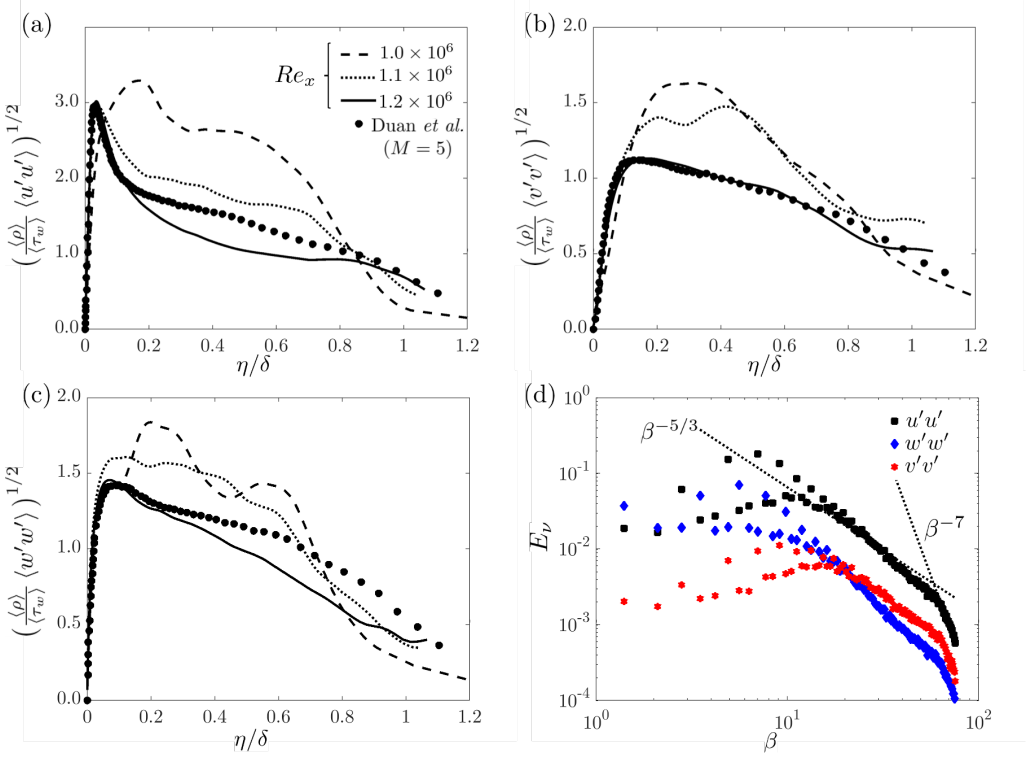


FIGURE 22. The wall-normal profiles of mean (a) streamwise velocity and (b) temperature.

FIGURE 23. The wall-normal profiles of density weighted RMS values of (a) streamwise; (b) wall-normal; and (c) spanwise velocity fluctuations at different Reynolds numbers. (d) Energy spectrum as a function of spanwise wavenumber β at $Re_x = 1.2 \times 10^6$.

1.2×10^6 and $\eta^+ = 40$. At this location, the energy spectrum of streamwise velocity fluctuations clearly exhibits an inertial and a dissipative subrange features, indicating that the flow is approaching a fully turbulent stage.

Our DNS also provides data for evaluating non-dimensional parameters which can be utilized for low-complexity modeling of high-speed compressible turbulent flows using time-averaged NS equations (Hirsch 2007). In particular, we examine the spatial evolution of fluctuation Mach number, M_t , fluctuation Prandtl number, Pr_t , and Huang's modified

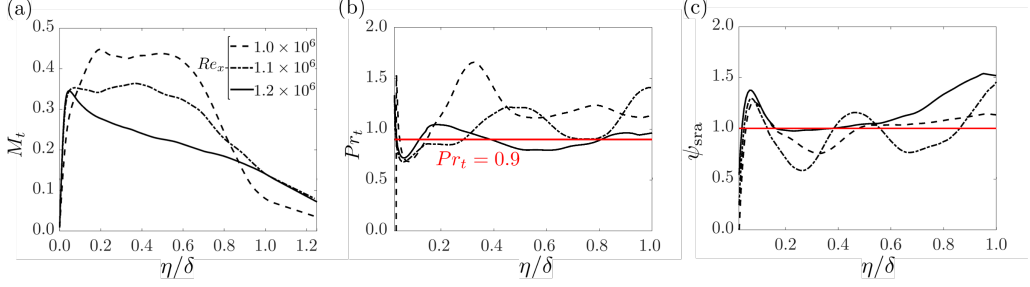


FIGURE 24. The wall-normal profiles of (a) fluctuation Mach number, M_t ; (b) fluctuation Prandtl number, Pr_t ; and (c) Huang's modified strong Reynolds analogy parameter, ψ_{sra} .

strong Reynolds analogy parameter (Huang *et al.* 1995), ψ_{sra} ,

$$M_t = \sqrt{\frac{\langle u'_i u'_i \rangle}{\gamma R \langle T \rangle}}, \quad Pr_t = \frac{\langle u'v' \rangle}{\langle v'T' \rangle} \frac{\partial_\eta \langle T \rangle}{\partial_\eta \langle u \rangle}, \quad \psi_{sra} = \frac{(1 - \frac{\partial \langle T_0 \rangle}{\partial \langle T \rangle}) Pr_t}{(\gamma - 1) \langle M \rangle^2} \frac{\langle u \rangle}{\langle T \rangle} \frac{T'_{rms}}{u'_{rms}}. \quad (6.5)$$

Here, $\langle u'_i u'_i \rangle = \langle u'u' \rangle + \langle v'v' \rangle + \langle w'w' \rangle$, γ and R denote the specific heat ratio and the gas constant, respectively, and T_0 is the stagnation temperature. In a fully developed turbulent boundary layer, ψ_{sra} provides a measure of correlation between velocity and temperature fluctuations (Huang *et al.* 1995).

Figure 24 shows that towards the end of the computational domain, at $Re_x = 1.2 \times 10^6$, these parameters are close to those observed in canonical hypersonic boundary layers, i.e., $M_t \approx 0.2 - 0.3$, $Pr_t \approx 0.9$, and $\psi_{sra} \approx 1$ (Pirozzoli & Bernardini 2011). However, upstream of the breakdown region, at $Re_x = 1.0 \times 10^6$, there is a significant deviation compared to these canonical values. Here, M_t becomes as high as 0.45 which suggests that compressibility effects on flow fluctuations cannot be neglected in the transition zone. Similarly, Pr_t can reach values close to 1.5 which correspond to decreased fluctuation temperature fluxes in the breakdown region. Furthermore, Pr_t exhibits large variations away from the wall, which is in contrast to the observations in flat-plate turbulent boundary layers, where Pr_t has value of 0.9 throughout the boundary layer (Saffman & Wilcox 1974; Smith & Smits 1993; Pirozzoli & Bernardini 2011). Similar deviations from canonical values in the outer region of boundary layer are also observed in ψ_{sra} . We conjecture that, in the presence of persistent upstream excitations, the resulting unsteady fluctuations are primarily responsible for these discrepancies.

7. Discussion

Recent experimental studies of hypersonic flows over axisymmetric compression corners (Benitez *et al.* 2020) and cone flares (Butler & Laurence 2021) identified the presence of unsteady fluctuations in the separation zone. It has been postulated that these fluctuations play an important role in initiating transition to turbulence downstream. As demonstrated in figure 25, we observe strong qualitative similarity between spatial structures of fluctuations observed using schlieren measurements in Mach 6 reattaching flow on axisymmetric cone-flare (Butler & Laurence 2021) and dominant oblique density fluctuations resulting from input-output analysis of separated flow over a slender double-wedge. Inspired by these observations, we examine transition mechanisms in a Mach 5 hypersonic flow over a slender double-wedge subject to unsteady upstream disturbances.

To investigate the early stages of transition, we quantify amplification of small external disturbances that are introduced upstream of the separation zone. We employ input-

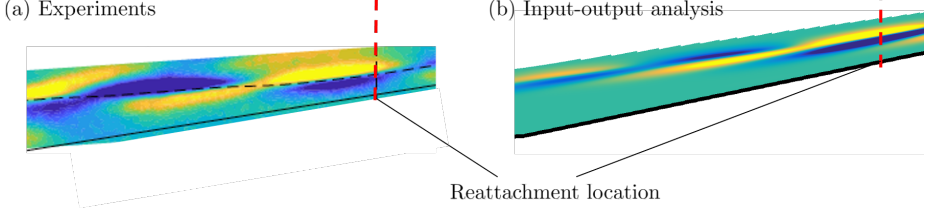


FIGURE 25. Qualitative comparison of spatial structures of (a) unsteady fluctuations observed using schlieren measurements in Mach 6 reattaching flow on axisymmetric cone-flare (Butler & Laurence 2021); and (b) dominant oblique density fluctuations resulting from input-output analysis of linearization around laminar 2D Mach 5 reattaching flow.

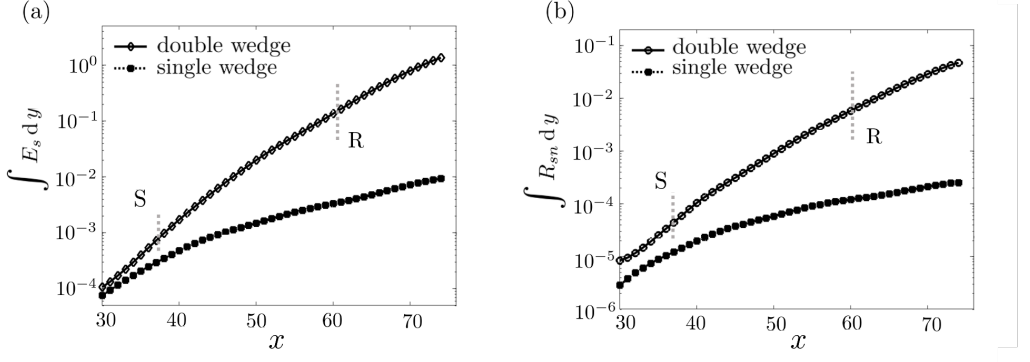


FIGURE 26. The streamwise evolution of (a) streamwise specific energy and (b) fluctuation shear stress of the dominant output mode ϕ_1 of the resolvent associated with linearization around laminar flows over double- and single-wedges with $(\omega = 0.4, \lambda_z = 3.0)$.

output analysis (Jovanović 2021) to evaluate response of a laminar flow to exogenous time periodic disturbances. This allows us to identify prevailing spatio-temporal scales, the spatial structure of inputs that most effectively excite the double-wedge flow, as well as the resulting output profiles. Input-output framework was successfully utilized to study transition mechanisms in numerous canonical flow configurations (e.g., see Jovanović & Bamieh (2005); Bagheri *et al.* (2009); Sipp & Marquet (2013); Ran *et al.* (2019a)). Here, we carry out input-output analysis of global compressible linearized dynamics and quantify amplification of flow fluctuations in the presence of high-speed flow separation.

Even though the underlying laminar flow is globally stable (Sidharth *et al.* 2018), input-output analysis demonstrates significant amplification of upstream external disturbances. Two types of disturbances are strongly amplified by the linearized dynamics: steady streamwise vortices and unsteady oblique waves. Dwivedi *et al.* (2019) conducted a study of steady vortical disturbances and the resulting reattachment streaks but amplification of unsteady disturbances and the evolution of flow fluctuations in a separation-reattachment zone have not been previously investigated. Even though the role of unsteady perturbations in similar flows has been recently examined, these studies either involve globally unstable flows (Cao *et al.* 2021) or they focus on the response of the upstream boundary layer to oblique waves (Lugrin *et al.* 2021). In contrast, we identify unsteady perturbations that are selectively amplified in the separation-reattachment zone.

Our analysis of fluctuations' kinetic energy in a streamline-aligned orthogonal coordinate system allows us to identify physical mechanisms responsible for amplification

of oblique waves in the separating and the reattaching boundary layer. Large energy amplification arises from the growth of the perturbation shear stress due to streamline curvature in the separated shear layer. This is in contrast to the attached boundary layers, where no such mechanism exists. To compare separated and attached boundary layers, we also conduct input-output analysis of the flow over a wedge that does not contain the compression corner (this wedge is identical to the first wedge in the double-wedge configuration analyzed in the paper). Figure 26 demonstrates that the presence of a recirculation zone in the double-wedge flow significantly increases amplification relative to the single-wedge flow. The amplification profile of the perturbation stress is significantly different in these two cases because of fundamentally different physical mechanisms.

As numerical studies of attached compressible boundary layers (Chang & Malik 1994; Fasel *et al.* 1993; Mayer *et al.* 2011) demonstrate, oblique waves lead to the formation of spanwise periodic streaks. To investigate different stages of transition to turbulence in the presence of unsteady oblique disturbances in separated high-speed flows, we also evaluate their nonlinear evolution. In particular, we utilize a weakly nonlinear analysis to show that the resolvent operator associated with the linearized dynamics governs the evolution of steady streaks that arise from quadratic interactions of unsteady oblique waves. We demonstrate that these quadratic interactions generate vortical excitations in the reattaching shear layer which lead to the formation of streaks in the recirculation zone and their subsequent amplification downstream. Additionally, we utilize SVD of the resolvent to demonstrate that the streaks can be well approximated by the second output mode. Similar to the most amplified steady output (Dwivedi *et al.* 2019), our analysis of the energy budget shows that deceleration of base flow near reattachment is responsible for amplification of reattachment streaks associated with this sub-optimal mode.

We also employ DNS to examine latter stages of nonlinear evolution of flow fluctuations. In the presence of strong upstream oblique disturbances, steady streaks saturate after reattachment and experience sinuous sub-harmonic oscillations. The resulting 3D boundary layer develops staggered patterns of lambda vortices which introduce regions of considerable local shear and lead to the emergence of fluctuations with higher spanwise wavenumbers and temporal frequencies. At this stage, the mean flow profile develops multiple inflection points (e.g., see Hall & Horseman 1991; Yu & Liu 1994; Reddy *et al.* 1998) and the laminar boundary layer starts to breakdown to turbulence. As the flow undergoes transition, the wall friction increases rapidly before settling to values predicted by turbulent correlations. This increase in wall friction is accompanied by an overshoot in the mean wall temperature within the transition zone. Overshoot in heat flux has been observed in prior experimental (Holden 1972; Wadhams *et al.* 2008) and numerical (Franko & Lele 2013) studies of transition in hypersonic boundary layers. In our study, overshoot arises from the changes in the ability of transitioning boundary layer to entrain fluid closer to the wall because of streak breakdown. This process disrupts transport of cold fluid to the wall and increases wall temperatures. Post-breakdown, our DNS shows that the boundary layer develops mean profile and fluctuation statistics that agree well with observations made in attached hypersonic turbulent boundary layers. We also utilize data resulting from our simulation to evaluate parameters that are important for transition modeling in RANS, e.g., the fluctuation Prandtl number and Mach number (Hirsch 2007). In the transition zone these parameters differ significantly from their fully developed turbulent values, thereby suggesting that more detailed modeling of transitional hypersonic flows over compression corners is required.

In summary, we have utilized input-output analysis to demonstrate significant amplification of upstream unsteady disturbances in a hypersonic flow over a double-wedge. These disturbances induce oblique flow fluctuations whose nonlinear interactions lead to

the appearance of steady streamwise streaks in a separation-reattachment zone. Streaks saturate nonlinearly after reattachment, undergo sinuous sub-harmonic oscillations, and eventually breakdown to turbulence. Unsteady disturbances in hypersonic boundary layers can arise from free-stream turbulence in wind tunnel experiments (Schneider 2001, 2015) as well as from upstream surface roughness (Schneider 2008), atmospheric particulates associated with ice-clouds and volcanic dust (Turco 1992; Chuvakhov *et al.* 2019), and atmospheric turbulence (Bushnell 1990). Novel physical mechanisms that we identify are unique to high-speed boundary layers with a separation-reattachment zone. We expect that insights about transition mechanisms that we provide (using a combination of input-output analysis, weakly-nonlinear analysis, and DNS) will guide the development of low-complexity models for fast and accurate prediction of transition in hypersonic flows under realistic in-flight conditions.

8. Concluding remarks

The slender double-wedge geometry is a canonical high-speed compressible flow configuration that is often employed in experimental and numerical studies of hypersonic boundary layers that separate at compression corners. The presence of a recirculation zone and separation-reattachment shocks increases sensitivity of a laminar flow to external disturbances and makes transition possible even in the absence of global instabilities (Dwivedi 2020). While the role of unsteady perturbations in triggering transition in attached high-speed boundary layers has been studied (Mayer *et al.* 2011; Hartman *et al.* 2021), mechanisms that facilitate amplification and breakdown in hypersonic double-wedge flow subject to unsteady external disturbances are not well understood. In this paper, we utilize input-output and weakly nonlinear analyses to identify amplification mechanisms in separated-reattaching boundary layers. We also use DNS to validate our predictions and provide additional insight into latter stages of transition to turbulence.

We briefly summarize the most important conclusions of our study.

- (i) Streamline curvature in the separation zone introduces selective amplification of oblique fluctuations in the presence of unsteady upstream external disturbances. The oblique waves are strongly amplified in a narrow band of temporal frequencies, around $\omega \approx 0.4$, over a broader range of spanwise wavelengths, $\lambda_z \in (2.5, 6)$.
- (ii) Quadratic interactions of oblique waves introduce streamwise vortices in the reattaching shear layer and lead to the formation of steady streaks. Deceleration of base flow near reattachment is primary driver for amplification of streaks in the recirculation zone.
- (iii) Direct numerical simulations demonstrate that the onset of transition is marked by sinuous motion of streaks and subsequent appearance of staggered patterns of lambda vortices. Broadband temporal fluctuations develop prior to the streak breakdown.
- (iv) There is a significant difference between the fluctuation Prandtl and Mach numbers in the transition zone compared to their fully developed turbulent values downstream.

Our work combines input-output and weakly nonlinear analyses with DNS to provide detailed characterization of amplification of unsteady upstream disturbances in a hypersonic shock/boundary layer interaction over a slender double-wedge. We demonstrate that primary amplification of oblique waves leads to secondary amplification of reattachment streaks in the recirculation zone, their subsequent breakdown, and transition to turbulence downstream. We expect that our results will motivate a systematic evaluation of specific disturbance environments that appear in wind tunnels or free flights and pave the way for the development of predictive transition models for hypersonic vehicles.

Acknowledgments

We would like to thank Graham V. Candler for providing access to the US3D solver and computational facilities at the University of Minnesota and the Air Force Office of Scientific Research for financial support under Award FA9550-18-1-0422.

Declaration of interests

The authors report no conflict of interest.

Appendix A. Compressible energy norm

We utilize compressible energy norm (Chu 1965; Hanifi *et al.* 1996)

$$\|\cdot\|_E^2 = \int_{\Omega} \left(\frac{\bar{\rho}}{2} |\mathbf{u}'|^2 + \frac{\bar{p}}{2\bar{\rho}^2} \rho'^2 + \frac{\bar{\rho}C_v}{2T} T'^2 \right) d\Omega, \quad (\text{A } 1)$$

to quantify energy of flow fluctuations, where $(\bar{p}, \bar{\rho}, \bar{T})$ denote pressure, density, and temperature of the base flow and C_v is specific heat at constant volume in the domain Ω .

Appendix B. Energy transport equation in streamline coordinates

The terms on the right-hand side of transport equation (3.10) for streamwise specific kinetic energy $\mathcal{E}_s := u'_s u'_s$ are determined by

$$\begin{aligned} \text{Production: } \mathcal{P} &:= -u'_s u'_n \partial_n \bar{u}_s - u'_s u'_s \partial_s \bar{u}_s - \rho' u'_s \frac{\bar{u}_s}{\bar{\rho}} \partial_s \bar{u}_s, \\ \text{Source: } \mathcal{S} &:= -\frac{u'_s}{\bar{\rho}} \partial_s p', \\ \text{Viscous: } \mathcal{V} &:= \frac{\bar{\mu}}{\bar{\rho}} (2u'_s \partial_s u'_s + u'_s \partial_n (\partial_n u'_s + \partial_s u'_n) + \partial_z u'_s (\partial_s w' + \partial_z u'_s)), \\ \text{Curvature: } \mathcal{C} &:= -K_c u'_s u'_n - \frac{2\bar{\mu}}{\bar{\rho} \bar{u}_s^2} (K_s^2 u'_s u'_n + K_c^2 u'_s u'_s) + \\ &\quad \frac{1}{\bar{\rho}} \left(u'_s \partial_s \left(\frac{2\bar{\mu} K_c u'_n}{\bar{u}_s} \right) - u'_s \partial_n \left(\frac{\bar{\mu} (K_c u'_s + K_s u'_n)}{\bar{u}_s} \right) \right) + \\ &\quad \frac{2\bar{\mu}}{\bar{u}_s \bar{\rho}} (K_s u'_s \partial_s u'_s + K_c u'_s (\partial_n u'_s + \partial_s u'_n) - K_s u'_s \partial_n u'_n). \end{aligned} \quad (\text{B } 1)$$

Here, K_c and K_s denote contributions arising from the curvature normal to the streamlines and from deceleration along the streamline direction, respectively, and $\bar{\mu}$ is the coefficient of viscosity associated with the laminar base flow.

Appendix C. Transport equation for the fluctuation shear stress

The transport equation that governs the evolution of time and spanwise averaged fluctuation shear stress $R_{sn} := \langle u'_s u'_n \rangle$ in (s, n, z) coordinates is given by

$$\bar{u}_s \frac{\partial R_{sn}}{\partial s} = P_r + S_r + C_r. \quad (\text{C } 1)$$

The viscous terms are neglected because they do not contribute to the transport of R_{sn} and the terms on the right-hand-side are determined by

$$\begin{aligned}
\text{Production: } P_r &:= -R_{sn}\partial_s \bar{u}_s - \langle u'_n u'_n \rangle \partial_n \bar{u}_s + \langle \rho' u'_s \rangle \frac{\partial_n \bar{p}}{\bar{\rho}^2} + \langle \rho' u'_n \rangle \frac{\partial_s \bar{p}}{\bar{\rho}^2}, \\
\text{Source: } S_r &:= -\frac{1}{\bar{\rho}} (\langle u'_n \partial_s p' \rangle + \langle u'_s \partial_n p' \rangle), \\
\text{Curvature: } C_r &:= (2E_s - \langle u'_n u'_n \rangle) K_c - R_{sn} K_s.
\end{aligned} \tag{C 2}$$

Appendix D. Nonlinear terms at $\mathcal{O}(\epsilon^2)$

As shown in § 4.1, $\mathcal{N}^{(2)}$ accounts for quadratic interactions between $\mathbf{U}_+^{(1)}$ and $\mathbf{U}_-^{(1)}$ at $\mathcal{O}(\epsilon^2)$. For steady streaks, the contributions to the mass $\rho^{(2)}$, velocity $\mathbf{u}^{(2)}$, and temperature $T^{(2)}$ equations in (4.5) are given by,

$$\begin{aligned}
\mathbf{N}_{\text{streak},\rho}^{(2)} &= -\mathbf{u}_+^{(1)} \cdot \nabla \rho_-^{(1)} - \mathbf{u}_-^{(1)} \cdot \nabla \rho_+^{(1)} - \rho_+^{(1)} \nabla \cdot \mathbf{u}_-^{(1)} - \rho_-^{(1)} \nabla \cdot \mathbf{u}_+^{(1)}, \\
\mathbf{N}_{\text{streak},\mathbf{u}}^{(2)} &= -\frac{\rho_-^{(1)} \partial_t \mathbf{u}_+^{(1)}}{\rho^{(0)}} - \frac{\rho_+^{(1)} \partial_t \mathbf{u}_-^{(1)}}{\rho^{(0)}} - \mathbf{u}_-^{(1)} \cdot \nabla \mathbf{u}_+^{(1)} - \mathbf{u}_+^{(1)} \cdot \nabla \mathbf{u}_-^{(1)} - \\
&\quad \frac{\rho_+^{(1)}}{\rho^{(0)}} \left((\mathbf{u}_-^{(1)} \cdot \nabla) \mathbf{u}^{(0)} + (\mathbf{u}^{(0)} \cdot \nabla) \mathbf{u}_-^{(1)} \right) - \\
&\quad \frac{\rho_-^{(1)}}{\rho^{(0)}} \left((\mathbf{u}_+^{(1)} \cdot \nabla) \mathbf{u}^{(0)} + (\mathbf{u}^{(0)} \cdot \nabla) \mathbf{u}_+^{(1)} \right), \\
\mathbf{N}_{\text{streak},T}^{(2)} &= -\mathbf{u}_-^{(1)} \cdot \nabla T_+^{(1)} - \mathbf{u}_+^{(1)} \cdot \nabla T_-^{(1)} + \frac{\tau_+^{(1)} : \nabla \mathbf{u}_-^{(1)} + \tau_-^{(1)} : \nabla \mathbf{u}_+^{(1)}}{\rho^{(0)}} + \\
&\quad (1 - \gamma) \left(T_-^{(1)} (\nabla \cdot \mathbf{u}_+^{(1)}) + T_+^{(1)} (\nabla \cdot \mathbf{u}_-^{(1)}) \right) - \\
&\quad \frac{2\rho_-^{(1)} \rho_+^{(1)}}{(\rho^{(0)})^2} \left(C_v (\mathbf{u}^{(0)} \cdot \nabla T^{(0)}) + \frac{p^{(0)} \nabla \cdot \mathbf{u}^{(0)}}{\rho^{(0)}} \right) - \\
&\quad C_v \frac{\rho_+^{(1)}}{\rho^{(0)}} \left(\partial_t T_-^{(1)} + \mathbf{u}^{(0)} \cdot \nabla T_-^{(1)} + \mathbf{u}_-^{(1)} \cdot \nabla T^{(0)} \right) - \\
&\quad \frac{\rho_+^{(1)}}{\rho^{(0)}} \frac{p^{(0)} \nabla \cdot \mathbf{u}_-^{(1)} + p_-^{(1)} \nabla \cdot \mathbf{u}^{(0)}}{\rho^{(0)}} - \\
&\quad C_v \frac{\rho_-^{(1)}}{\rho^{(0)}} \left(\partial_t T_+^{(1)} + \mathbf{u}^{(0)} \cdot \nabla T_+^{(1)} + \mathbf{u}_+^{(1)} \cdot \nabla T^{(0)} \right) - \\
&\quad \frac{\rho_-^{(1)}}{\rho^{(0)}} \frac{p^{(0)} \nabla \cdot \mathbf{u}_+^{(1)} + p_+^{(1)} \nabla \cdot \mathbf{u}^{(0)}}{\rho^{(0)}}.
\end{aligned} \tag{D 1}$$

Here, $C_v = R/(\gamma - 1)$, where R is the gas constant, $\gamma = 1.4$ is the ratio of the specific heat capacities, and $\tau = -\frac{2}{3} \mu \delta_{ij} \nabla \cdot \mathbf{u} + \mu (\partial_i \mathbf{u}_j + \partial_j \mathbf{u}_i)$ is the second order deviatoric stress tensor where i and j stand for x , y , or z . In the indicial notation, $(\tau : \nabla \mathbf{u}) := \tau_{ij} \partial_j u_i$, and standard convention of summation over repeated indices is applied.

REFERENCES

- BAGHERI, S., BRANDT, L. & HENNINGSON, D. S. 2009 Input-output analysis, model reduction and control of the flat-plate boundary layer. *J. Fluid Mech.* **620**, 263–298.
- BENITEZ, E. K., ESQUIEU, S., JEWELL, J. S. & SCHNEIDER, S. P. 2020 Instability measurements on an axisymmetric separation bubble at Mach 6. In *AIAA aviation 2020 forum*. AIAA 2020-3072.
- BERLIN, S. & HENNINGSON, D. S. 1999 A nonlinear mechanism for receptivity of free-stream disturbances. *Phys. Fluids* **11** (12), 3749–3760.
- BERLIN, S., WIEGEL, M. & HENNINGSON, D. S. 1999 Numerical and experimental investigations of oblique boundary layer transition. *J. Fluid Mech.* **393**, 23–57.
- BUSHNELL, D. 1990 Notes on initial disturbance fields for the transition problem. In *Instability and transition*, pp. 217–232. Springer.
- BUTLER, C. S. & LAURENCE, S. J. 2021 Interaction of second-mode disturbances with an incipiently separated compression-corner flow. *J. Fluid Mech.* **913**, R4.
- CANDLER, G. V., JOHNSON, H. B., NOMPILIS, I., GIDZAK, V. M., SUBBAREDDY, P. K. & BARNHARDT, M. 2015 Development of the US3D code for advanced compressible and reacting flow simulations. In *53rd AIAA Aerospace Sciences Meeting*. AIAA 2015-1893.
- CAO, S., HAO, J., KLIOUTCHNIKOV, I., OLIVIER, H. & WEN, C. Y. 2021 Unsteady effects in a hypersonic compression ramp flow with laminar separation. *J. Fluid Mech.* **912**, A3.
- CHANG, C.-L. & MALIK, M. R. 1994 Oblique-mode breakdown and secondary instability in supersonic boundary layers. *J. Fluid Mech.* **273**, 323–360.
- CHOMAZ, J-MARC 2005 Global instabilities in spatially developing flows: non-normality and nonlinearity. *Annu. Rev. Fluid Mech.* **37**, 357–392.
- CHOUDHARI, M. 1996 Boundary-layer receptivity to three-dimensional unsteady vortical disturbances in free stream. In *AIAA*. AIAA Paper 96-0181.
- CHU, B.-T 1965 On the energy transfer to small disturbances in fluid flow (Part I). *Acta Mech.* **1** (3), 215–234.
- CHUVAKHOV, P. V., BOROVY, V. Y., EGOROV, I. V., RADCHENKO, V. N., OLIVIER, H. & ROGHELIA, A. 2017 Effect of small bluntness on formation of Görtler vortices in a supersonic compression corner flow. *J. Appl. Mech. Tech. Phys.* **58** (6), 975–989.
- CHUVAKHOV, P. V., FEDOROV, A. V. & OBRAZ, A. O. 2019 Numerical modelling of supersonic boundary-layer receptivity to solid particulates. *J. Fluid Mech.* **859**, 949–971.
- DOLLING, D. S. 2001 Fifty years of shock-wave/boundary-layer interaction research: what next? *AIAA J.* **39** (8), 1517–1531.
- DUAN, L., BEEKMAN, I. & MARTÍN, M. P. 2011 Direct numerical simulation of hypersonic turbulent boundary layers. Part 3. Effect of Mach number. *J. Fluid Mech.* **672**, 245–267.
- DWIVEDI, A. 2020 Global input-output analysis of flow instabilities in high-speed compressible flows. PhD thesis, University of Minnesota.
- DWIVEDI, A., BROSŁAWSKI, C. J., CANDLER, G. V. & BOWERSOX, R. D. 2020a Three-dimensionality in shock/boundary layer interactions: a numerical and experimental investigation. In *AIAA AVIATION 2020 FORUM*. AIAA 2020-3011.
- DWIVEDI, A., HILDEBRAND, N., NICHOLS, J. W., CANDLER, G. V. & JOVANOVIĆ, M. R. 2020b Transient growth analysis of oblique shock-wave/boundary-layer interactions at Mach 5.92. *Phys. Rev. Fluids* **5** (6), 063904.
- DWIVEDI, A., NICHOLS, J. W., JOVANOVIĆ, M. R. & CANDLER, G. V. 2017 Optimal spatial growth of streaks in oblique shock/boundary layer interaction. In *8th AIAA Theoretical Fluid Mechanics Conference*. AIAA 2017-4163.
- DWIVEDI, A., SIDHARTH, G. S., NICHOLS, J. W., CANDLER, G. V. & JOVANOVIĆ, M. R. 2019 Reattachment vortices in hypersonic compression ramp flow: an input-output analysis. *J. Fluid Mech.* **880**, 113–135.
- FASEL, H. F., THUMM, A. & BESTEK, H. 1993 Direct numerical simulation of transition in supersonic boundary layers: oblique breakdown. In *Fluids Engineering Conference*, pp. 77–92.
- FINNIGAN, J. J. 1983 A streamline coordinate system for distorted two-dimensional shear flows. *J. Fluid Mech.* **130**, 241–258.
- FRANKO, K. J. & LELE, S. K. 2013 Breakdown mechanisms and heat transfer overshoot in hypersonic zero pressure gradient boundary layers. *J. Fluid Mech.* **730**, 491.

- HADER, C. & FASEL, H. F. 2019 Direct numerical simulations of hypersonic boundary-layer transition for a flared cone: fundamental breakdown. *J. Fluid Mech.* **869**, 341–384.
- HALL, P. & HORSEMAN, N. J. 1991 The linear inviscid secondary instability of longitudinal vortex structures in boundary layers. *J. Fluid Mech.* **232**, 357–375.
- HANIFI, A., SCHMID, P. J. & HENNINGSON, D. S. 1996 Transient growth in compressible boundary layer flow. *Phys. Fluids* **8** (3), 826–837.
- HARTMAN, A. B., HADER, C. & FASEL, H. F. 2021 Nonlinear transition mechanism on a blunt cone at Mach 6: oblique breakdown. *J. Fluid Mech.* **915**, R2.
- HILDEBRAND, N., DWIVEDI, A., NICHOLS, J. W., JOVANOVIĆ, M. R. & CANDLER, G. V. 2018 Simulation and stability analysis of oblique shock-wave/boundary-layer interactions at Mach 5.92. *Phys. Rev. Fluids* **3**, 013906 (23 pages).
- HIRSCH, C. 2007 *Numerical computation of internal and external flows: The fundamentals of computational fluid dynamics*. Elsevier.
- HODA, N., JOVANOVIĆ, M. R. & KUMAR, S. 2008 Energy amplification in channel flows of viscoelastic fluids. *J. Fluid Mech.* **601**, 407–424.
- HODA, N., JOVANOVIĆ, M. R. & KUMAR, S. 2009 Frequency responses of streamwise-constant perturbations in channel flows of Oldroyd-B fluids. *J. Fluid Mech.* **625**, 411–434.
- HOLDEN, M. S. 1972 An experimental investigation of turbulent boundary layers at high Mach number. *NASA Contractor Rep.* **111242**.
- HUANG, P. G., COLEMAN, G. N. & BRADSHAW, P. 1995 Compressible turbulent channel flows: DNS results and modelling. *J. Fluid Mech.* **305**, 185–218.
- JEUN, J., NICHOLS, J. W. & JOVANOVIĆ, M. R. 2016 Input-output analysis of high-speed axisymmetric isothermal jet noise. *Phys. Fluids* **28** (4), 047101.
- JOVANOVIĆ, M. R. 2004 Modeling, analysis, and control of spatially distributed systems. PhD thesis, University of California, Santa Barbara.
- JOVANOVIĆ, M. R. 2021 From bypass transition to flow control and data-driven turbulence modeling: An input-output viewpoint. *Annu. Rev. Fluid Mech.* **53** (1), 311–345.
- JOVANOVIĆ, M. R. & BAMIEH, B. 2005 Componentwise energy amplification in channel flows. *J. Fluid Mech.* **534**, 145–183.
- JOVANOVIĆ, M. R. & KUMAR, S. 2011 Nonmodal amplification of stochastic disturbances in strongly elastic channel flows. *J. Non-Newtonian Fluid Mech.* **166** (14–15), 755–778.
- LUGRIN, M., BENEDDINE, S., LECLERCQ, C., GARNIER, E. & BUR, R. 2021 Transition scenario in hypersonic axisymmetrical compression ramp flow. *J. Fluid Mech.* **907**, A6.
- MA, Y. & ZHONG, X. 2005 Receptivity of a supersonic boundary layer over a flat plate. Part 3. Effects of different types of free-stream disturbances. *J. Fluid Mech.* **532**, 63.
- MASLOV, A. A., SHIPLYUK, A. N., SIDORENKO, A. A. & ARNAL, D. 2001 Leading-edge receptivity of a hypersonic boundary layer on a flat plate. *J. Fluid Mech.* **426**, 73.
- MAYER, C. S. J., VON TERZI, D. A. & FASEL, H. F. 2011 Direct numerical simulation of complete transition to turbulence via oblique breakdown at Mach 3. *J. Fluid Mech.* **674**, 5.
- NAVARRO-MARTINEZ, S. & TUTTY, O. R. 2005 Numerical simulation of Görtler vortices in hypersonic compression ramps. *Comput. Fluids* **34** (2), 225–247.
- NOMPELIS, I. & CANDLER, G. V. 2009 Numerical investigation of double-cone flows with high enthalpy effects. *ESASP* **659**, 96.
- NOMPELIS, I., CANDLER, G. V. & HOLDEN, M. S. 2003 Effect of vibrational nonequilibrium on hypersonic double-cone experiments. *AIAA J.* **41** (11), 2162–2169.
- PATEL, V. C. & SOTIROPOULOS, F. 1997 Longitudinal curvature effects in turbulent boundary layers. *Prog. in Aerospace Sci.* **33** (1–2), 1–70.
- PIROZZOLI, S. & BERNARDINI, M. 2011 Turbulence in supersonic boundary layers at moderate Reynolds number. *J. Fluid Mech.* **688**, 120.
- RAN, W., ZARE, A., HACK, M. J. P. & JOVANOVIĆ, M. R. 2019a Modeling mode interactions in boundary layer flows via Parabolized Floquet Equations. *Phys. Rev. Fluids* **4** (2), 023901 (22 pages).
- RAN, W., ZARE, A., HACK, M. J. P. & JOVANOVIĆ, M. R. 2019b Stochastic receptivity analysis of boundary layer flow. *Phys. Rev. Fluids* **4** (9), 093901 (28 pages).
- REDDY, S. C., SCHMID, P. J., BAGGETT, J. S. & HENNINGSON, D. S. 1998 On stability of

- streamwise streaks and transition thresholds in plane channel flows. *J. Fluid Mech.* **365**, 269–303.
- ROGHILIA, A., OLIVIER, H., EGOROV, I. & CHUVAKHOV, P. 2017 Experimental investigation of Görtler vortices in hypersonic ramp flows. *Exp. Fluids* **58** (10), 139.
- SAFFMAN, P. G. & WILCOX, D. C. 1974 Turbulence-model predictions for turbulent boundary layers. *AIAA J.* **12** (4), 541–546.
- SCHMID, P. J. 2007 Nonmodal stability theory. *Annu. Rev. Fluid Mech.* **39**, 129–162.
- SCHMID, P. J. & HENNINGSON, D. S. 1992 A new mechanism for rapid transition involving a pair of oblique waves. *Phys. of Fluids A: Fluid Dyn.* **4** (9), 1986–1989.
- SCHNEIDER, S. P. 2001 Effects of high-speed tunnel noise on laminar-turbulent transition. *J. Spacecr. Rockets* **38** (3), 323–333.
- SCHNEIDER, STEVEN P 2008 Effects of roughness on hypersonic boundary-layer transition. *J. Spacecr. Rockets* **45** (2), 193–209.
- SCHNEIDER, S. P. 2015 Developing mechanism-based methods for estimating hypersonic boundary-layer transition in flight: The role of quiet tunnels. *Prog. in Aero. Sc.* **72**, 17–29.
- SIDHARTH, G. S., DWIVEDI, A., CANDLER, G. V. & NICHOLS, J. W. 2017 Global linear stability analysis of high speed flows on compression ramps. In *47th AIAA Fluid Dynamics Conference*. AIAA 2017-3455.
- SIDHARTH, G. S., DWIVEDI, A., CANDLER, G. V. & NICHOLS, J. W. 2018 Onset of three-dimensionality in supersonic flow over a slender double wedge. *Phys. Rev. Fluids* **3** (9), 093901 (29 pages).
- SIMEONIDES, G. & HAASE, W. 1995 Experimental and computational investigations of hypersonic flow about compression ramps. *J. Fluid Mech.* **283**, 17–42.
- SIPP, D. & MARQUET, O. 2013 Characterization of noise amplifiers with global singular modes: the case of the leading-edge flat-plate boundary layer. *Theoretical and Computational Fluid Dynamics* **27** (5), 617–635.
- SIVASUBRAMANIAN, J. & FASEL, H. F. 2015 Direct numerical simulation of transition in a sharp cone boundary layer at Mach 6: fundamental breakdown. *J. Fluid Mech.* **768**, 175–218.
- SKINNER, S., BUTLER, C., LAURENCE, S. J. & MANGALAM, A. S. 2020 In-situ measurements of turbulent velocity, temperature, and acoustic fluctuations in the stratosphere. In *AIAA Scitech 2020 Forum*. AIAA, 2020-0778.
- SMITH, D. R. & SMITS, A. J. 1993 Simultaneous measurement of velocity and temperature fluctuations in the boundary layer of a supersonic flow. *Exp. Therm. Fluid Sc.* **7** (3), 221–229.
- SUBBAREDDY, P. K., BARTKOWICZ, M. D. & CANDLER, G. V. 2014 Direct numerical simulation of high-speed transition due to an isolated roughness element. *J. Fluid Mech.* **748**, 848–878.
- SUBBAREDDY, PRAMOD K & CANDLER, GRAHAM V 2009 A fully discrete, kinetic energy consistent finite-volume scheme for compressible flows. *J. Comput. Phys.* **228** (5), 1347–1364.
- SUBBAREDDY, P. K. & CANDLER, G. V. 2012 DNS of transition to turbulence in a Mach 6 boundary layer. In *43rd AIAA Thermophysics Conference*. AIAA, AIAA 2012-3106.
- TURCO, R. P. 1992 Upper-atmosphere aerosols: properties and natural cycles. *The Atmospheric Effects of Stratospheric Aircraft: A First Program Report* **1272**, 63.
- WADHAMS, T. P., MUNDY, E., MACLEAN, M. G. & HOLDEN, M. S. 2008 Ground test studies of the HIFiRE-1 transition experiment Part 1: Experimental results. *J. Spacecr. Rockets* **45** (6), 1134–1148.
- WHITE, F. M. & MAJDALANI, J. 2006 *Viscous fluid flow*, vol. 3. McGraw-Hill New York.
- YANG, L., ZARE-BEHTASH, H., ERDEM, E. & KONTIS, K. 2012 Investigation of the double ramp in hypersonic flow using luminescent measurement systems. *Exp. Therm. Fluid Sci.* **40**, 50–56.
- YU, X. & LIU, J.T.C. 1994 On the mechanism of sinuous and varicose modes in three-dimensional viscous secondary instability of nonlinear Görtler rolls. *Phys. Fluids* **6** (2), 736–750.